POLITECNICO
MILANO 1863

DIPARTIMENTO DI MECCANICA

mecc

Modeling and characterization of dynamic recrystallization under variable deformation states

Caiyi Liu, Silvia Barella, Yan Peng, Shuo Guo, Shicheng Liang, Jianliang Sun, Andrea Gruttadauria, Marco Belfi, Carlo Mapelli

This is a post-peer-review, pre-copyedit version of an article published in International Journal of Mechanical Sciences. The final authenticated version is available online at:
http://dx.doi.org/j.ijmecsci.2022.107838

DIPARTIMENTO DI MECCANICA ■ POLITECNICO DI MILANO
via G. La Masa, 1 ■ 20156 Milano ■ EMAIL (PEC): pecmecc@cert.polimi.it
http://www.mecc.polimi.it
Rev. 0

Modeling and characterization of dynamic recrystallization under variable deformation states

Caiyi Liu[a], Silvia Barella[b], Yan Peng[a,*], Shuo Guo[a], Shicheng Liang[a], Jianliang Sun[a], Andrea Gruttadauria[b], Marco Belfi[b], Carlo Mapelli[b]

[a] National Engineering Research Center for Equipment and Technology of Cold Strip Rolling, Yanshan University, Qinhuangdao 066004, China

[b] Department of Mechanical Engineering, Politecnico di Milano, Milan, 20156, Italy

[*] Correspondence: pengyan@ysu.edu.cn

Abstract: Flexible rolling with variable deformation states has brought new challenges to dynamic recrystallization (DRX) theory based on conventional constant deformation state. Modeling and characterization of DRX are investigated, inspired by the successful application of constitutive models and EBSD technique in the field of characterizing the recrystallization of metallic materials, combined with the characteristics of flow stress. Two constitutive models for constant and transient deformation states were considered. The dynamic recovery effect was integrated into the model for predicting the flow stress and DRX volume fraction. A hot processing map was established to predict the instability region. Various DRX synergistic regulation mechanisms and crystallographic orientation distribution under a transient deformation state were explored. The results suggest that DRX is the main softening characteristic under various deformation states. The predicted flow stress of the constant and transient models are in good agreement with the experimental values. The regulation mechanism of DRX transforms from continuous DRX to discontinuous DRX when the strain rate dynamic decreases. DRX grains display a random orientation distribution, and the crystallographic orientation is toward the ⟨111⟩ fiber parallel to the normal direction of the compression axis when the DRX volume fraction is high. These findings provide insight into the DRX constitutive description and microstructure evolution under variable deformation states.

Keywords: Dynamic recrystallization; Microstructure evolution; Hot workability; Variable deformation states

1 Introduction

The development of advanced forming and manufacturing technology (e.g., flexible rolling, ring rolling, and multidirectional forging) has posed new challenges in the investigation of dynamic recrystallization (DRX) of conventional metallic materials. For instance, in the flexible rolling inline work-roll change process, worn rolls are withdrawn and new rolls are launched into the rolling process, rolling speed and deformation temperature regulation of the process is needed among the mills. This causes strain rate and deformation temperature variation during the strip deformation process, and this will break the constant deformation process (i.e., at a constant strain rate or deformation temperature), causing the rolling process to change from a constant to a transient deformation state (i.e., at a dynamic strain rate or deformation temperature). Resulting in more complex softening behavior compared to the conventional DRX constant deformation state regulating procedure [1-3]. DRX is an important microstructure evolution behavior of metallic materials for thermomechanical processing, which determines the microstructure morphology and properties of the products. Therefore, it is crucial to investigate the DRX behavior under variable deformation states [4]. In recent years, many scholars have conducted studies on the recrystallization and thermomechanical processing of metallic materials. Li et al. physically simulated the DRX behavior and hot workability of 300M steel using the Gleeble 3500 physical simulation system. The result shows that the deformation speed and temperature are key variables impacting DRX behavior. The mechanism for the investigation of the coupling regulation of recrystallization and hot workability is established through the observation of the correlation between the power dissipation efficiency (PDE) and DRX behavior in the hot processing map (HPM) [5]. Zhao et al. developed power dissipation and instability maps to optimize the hot workability of 300M. The findings show that flow instability and PDE are strongly related, and PDE is susceptible to flow instability at the rate of less than 25% [6]. Zhang et al. explored the DRX behavior of aluminum alloys and analyzed the mechanism at various deformation temperatures. The result shows that two principal

DRX regulation mechanisms of aluminum alloys during hot deformation are discontinuous dynamic recrystallization (DDRX) and continuous dynamic recrystallization (CDRX) [7]. Xiao et al. evaluated the stress–strain characteristics and hot workability of titanium alloys during high-temperature plastic deformation, and the development of HPM at various deformation degrees. The results show that the factors important in regulating flow stress behavior are deformation temperature and strain rate [8].

Since DRX is the main softening mechanism during high-temperature plastic deformation process. Various kinetic models have been developed to quantify the DRX volume fraction under different deformation parameters. Sellars et al. conducted a pioneering investigation on the DRX behavior of metallic materials based on the Gleeble thermomechanical technique, and developed a time-dependent DRX kinetic model according to the Avrami function [9, 10]. On this basis, Yada et al. developed a strain-dependent DRX kinetic model [11]. When the strain rate is constant, the time function is the same as the strain function. Therefore, Sellars's model and Yada's model are the same in nature. However, since Yada's model uses the strain function, it can be applied in the nonlinear numerical simulation of metal plastic deformation. Thus, numerical simulation software generally uses Yada's model in the form of predicting metallic material recrystallization behavior. Kim et al. developed a new DRX kinetic model based on Yada's model and applied the DRX maximum rate instead of the state corresponding to the DRX volume fraction of 50% in the original equation [12, 13]. As the DRX velocity is slowly increasing from zero, and reaches the maximum DRX velocity corresponding to the 50% volume fraction of DRX. After reaching the maximum velocity of DRX gradually decreases. Therefore, both Kim's model and Yada's model have the same physical meaning regarding the DRX velocity. Liu et al. optimized the form of exponential functions of previous models and developed a new DRX kinetic model [14]. Jonas et al. conducted extensive studies on DRX and DRV critical strain determination, the microstructure transformation mechanisms, and established DRX kinetic models applicable to different steel materials [15, 16]. Nowadays, Jonas's model is widely used to analyze the variation of DRX volume fraction of different materials.

In tandem with transient deformation states, limited prior research have been conducted on the flow behavior of metals. Frommert and Graetz et al. studied DRX behavior under strain rate transient variation state. The findings reveal that the flow characteristics and recrystallization vary considerably in the process of strain rate transient variation. DRX behavior will fluctuate between the dynamic equilibrium stages under the transient variation state. However, the mechanism and regulation of DRX during strain rate transient variation are not understood [17, 18]. Based on previous studies, Chen et al. used the EBSD technique to reveal the microstructure evolution of the Ni-30%Fe alloy under strain rate transient variation state. The findings indicate that the DRX volume fraction for strain rate transient variations is between the maximum and minimum values at a constant strain rate state [19]. Wang et al. employed a kinetic model to explore the transient thermomechanical processing state induced by the strain rate transient jump. The microstructure evolution and deformation temperature transient variation are not studied [20]. In summary, recent studies mainly investigate DRX behavior and hot workability, respectively, or consider the effects of DRX behavior and hot workability at a specific deformation degree. However, the studies do not consider the coupled regulation of DRX behavior and HPM of materials during variable deformation states. The exploration of deformation speed and temperature transient variation is still relatively scarce, and the mechanism of the above two critical variables' transient variation process on the microstructure evolution and crystallographic orientation is still unclear. The work aims to investigate the DRX behavior and hot workability under variable deformation states to reveal the recrystallization mechanism, hot workability and coupling regulation of critical variables. These findings can provide an important theoretical basis for the regulation of DRX behavior of advanced forming and manufacturing technologies under variable deformation states.

2. Global experimental procedure

In this section, DRX behavior and hot workability experimental procedure of materials under variable deformation states are introduced. First, experimental steps and cautions for physical simulation under constant state and transient deformation states, the methodologies and techniques for analyzing the microstructure evolution are

described in Section 2.1. Then, the basis for the selection of metallic materials, its chemical composition, original microstructure are introduced in Section 2.2. Details of the experimental procedure will be explained next.

2.1. Experimental detail

The Gleeble 3800-GTC system is used to simulate various deformation states. The specimen is a cylindrical shape with a length of 12 mm and a diameter of 8 mm. The physical simulation was performed using uniaxial compression under argon gas protection. The test system automatically recorded the critical factors related to thermal deformation, such as stress, strain, and temperature during the single-pass hot compression experiment. Molybdenum disulfide lubricant, tantalum foil and graphite were applied between the sample and the indenter before the experiment to reduce friction and restrain sticking, promote stability and homogeneity during the compression test, maintain a consistent temperature along the length of the specimen. The K-type thermocouple was welded to the length center of the specimen to record temperature variations. Fig. 1(a) illustrates the global experimental procedure.

The first experimental scheme is a constant deformation state in which the samples were deformed at a constant deformation parameter in a single-pass hot compression test. Samples were heated to 1150℃ at a rate of 10℃/s, holding for 240s to homogenize the austenite phase, then cooled to the corresponding deformation temperature at a rate of 5℃/s, holding for 60s to reduce the temperature fluctuations, then compressed to a strain of 0.9 using the specific experimental parameters illustrated in Fig. 1(b).

The second experimental scheme is a transient deformation state in which the samples were compressed at deformation temperature or strain rate transient variation in a single-pass hot compression test. The samples were heated to 1150℃ at a rate of 10℃/s, holding for 240s to homogenize the austenite phase, then cooled to 1000℃ or 1100℃ at a rate of 5℃/s, holding for 60s to reduce the temperature fluctuations. The strain rate transient variation was divided into two parts, as shown in Fig. 1(c). In the first part, the specimen was first deformed to a strain of 0.4 before the strain rate dynamic increased, compressing the specimen to a strain of 0.5 and 0.9. In the second part, the specimen was first compressed to a strain of 0.4 before the strain rate dynamic decreased, compressing the specimen to a strain of 0.5 and 0.9. Likewise, the deformation temperature transient variation was divided into two parts, as illustrated in Fig. 1(d). In the first part, the specimen was first compressed to a strain of 0.4 at a deformation temperature of 1000℃, then the temperature transient jumps to 1100℃ at a rate of 10℃/s, compressing the specimen to a strain of 0.5 and 0.9. In the second part, the specimen was first compressed to a strain of 0.4 at a deformation temperature of 1100℃, then the temperature transient jumps to 1000℃ at a rate of 10℃/s, compressing the specimen to a strain of 0.5 and 0.9.

To freeze the high-temperature microstructure morphology of samples after a single-pass hot compression test, water quenching process was used to cool the samples after variable deformations. The Micracut 202 cutting machine was used to precisely split the quenched specimen along the axial direction of the contact surface with the indenter. The microstructure characterization was performed in the center of the cut specimen, concerning the normal direction (ND) and the extension direction (ED). Since the material used in this paper had lower stacking fault energies (SFE), the substructure did not form as readily during hot deformation as the higher SFE, which makes it difficult to statistically evaluate the substructure evolution using TEM [21]. Large area measurements were performed using the EBSD technique to quantify the microstructure evolution under variable deformation states. After mounting, grinding and mechanical polishing, the specimen was electrolytically polished with 6% perchloric acid and 94% acetic acid, with an electropolishing time of 15-20s, a current of 0.2-0.7A and an electropolishing temperature of 22℃. The EBSD technique was applied with a step size of 0.3-1.0 μm depending on the grain size and data quality of the sample under variable deformation states. Oxford AZtec and HKL Channel 5 were applied for data acquisition and processing, respectively. Grains with different misorientation angles are defined as low-angle grain boundaries (LAGBs) of 2° - 5°, medium-angle grain boundaries (MAGBs) of 5° - 15°, and high-angle grain boundaries (HAGBs) of higher than 15°. The three aforementioned boundaries are marked in green, blue and black solid lines in the grain boundary (GB)

map, respectively.

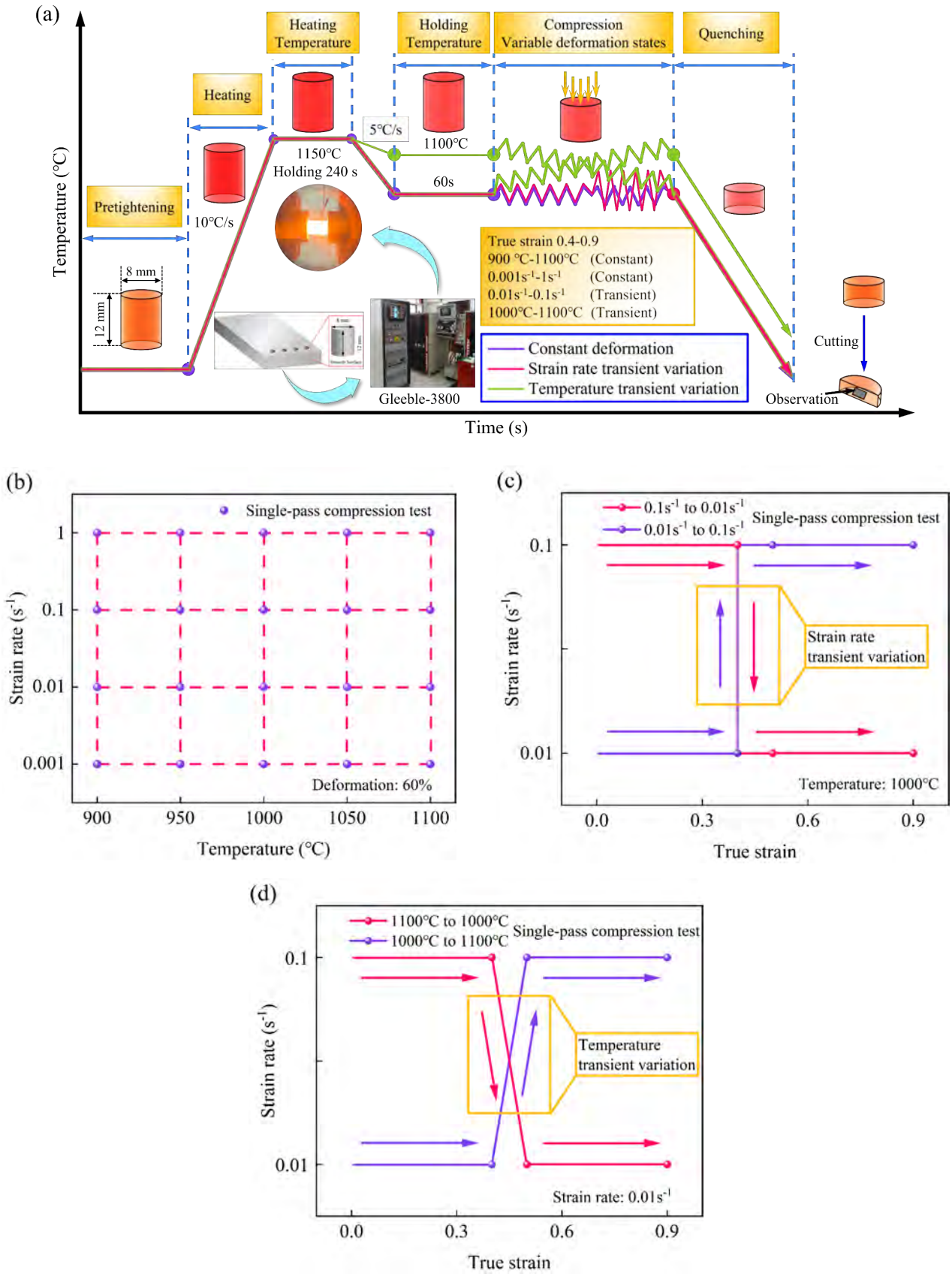

Fig. 1. Schematic of physical simulation of constant and transient deformation states: (a) temperature versus time for constant and transient deformation states, (b) constant strain rate and constant deformation temperature for constant deformation state, (c) constant deformation temperature and strain rate variation for transient deformation state, (d)

constant strain rate and deformation temperature variation for transient deformation state.

2.2. Experimental materials

Since prior austenite morphology in ASTM-316L can be kept stable at room temperature during thermomechanical processing. It can prevent phase transformation during the carbon steel quenching process from disturbing the prior austenite microstructure characterization, which facilitates the in-depth study of recrystallization under variable deformation states [22]. It is perfectly applicable to this paper to study the advanced forming technology under various deformation states and to observe the microstructure evolution behavior of prior austenite. Therefore, a commercially ASTM-316L plate was chosen to study the DRX behavior and hot workability under variable deformation states. Table 1 displays the composition of the experimental steel. Fig. 2(a) shows the original microstructure consisting of approximately equiaxed recrystallized grains and annealed twins. The average grain size was measured to be 26 μm. As the nucleation and homogenous development of recrystallized grains are characterized by random orientation at grain boundaries during heat treatment [23], the pole figures in Fig. 2(b) shows a weak microtexture before single-pass compression test.

Table 1. Composition of ASTM-316L (wt.%).

C	Si	Cr	Mn	P	S	Ni	Mo	N	Fe
0.022	0.58	16.64	1.49	0.026	0.001	10.08	2.09	0.036	Bal.

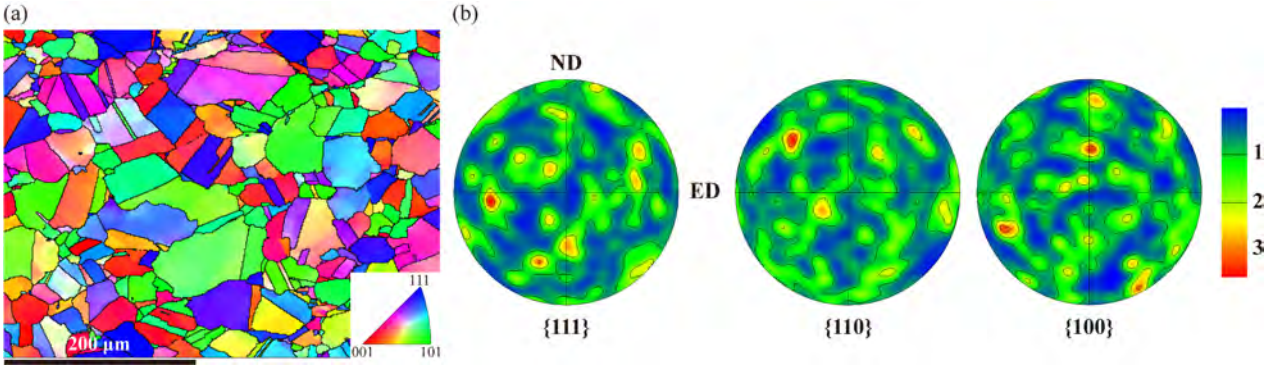

Fig. 2. Initial microstructure of specimen: (a) EBSD IPF color maps. (b) {111}, {110} and {100} pole figures concerning the normal direction (ND) and the extension direction (ED).

3. Results and discussion

This section presents the results and related discussions about DRX behavior and hot workability under constant and transient deformation states. Firstly, the flow stress curves of metallic materials at constant and transient deformation states is concerned. On this basis, the material constitutive model and DRX kinetic model are developed under a constant deformation state. By analyzing the special modeling methods for the flow stress and DRX kinetics in contrast to the traditional modeling methods for the constant deformation state, an appropriate constitutive model and DRX kinetic model for the transient deformation state are derived. Then, the hot workability of the material under current deformation conditions is evaluated, and the relationship between hot workability and microstructure evolution is established. Finally, the microstructure evolution and crystallographic orientation of the material under transient deformation state are analyzed.

3.1. Evolution of flow stress curves

3.1.1. Constant deformation state

Fig. 3 depicts the flow stress curves of 316L deformed at a constant deformation state. All curves' raw data were smoothed using MATLAB software. When the specimen deformed at a lower deformation temperature under a constant strain rate, the flow stress curves exhibited a DRV type and transferred to a DRX type as the temperature increased [24]. The maximum value of the flow stress changed with the deformation parameters. It decreased with rising temperature when the strain rate was constant. The flow stress curves exhibited a smoothing character close to

the maximum stress value at a higher temperature or lower strain rate. This smoothing characteristic correlated with the coordinated competitive timing between work hardening (WH) and dynamic softening (DS). The faster deformation at a higher strain rate and the slower GB migration rate at a lower temperature inhibited the DRX rate. Correspondingly, a longer time is needed to reach balance between WH and DS. Thus, a distinct flattening characteristic appeared close to the peak stress [25]. Fig. 3 also depicts that the steady stress increased slightly near the end of deformation as the increased contact zone between the sample and the indenter during the single-pass compression test induces increased friction [26].

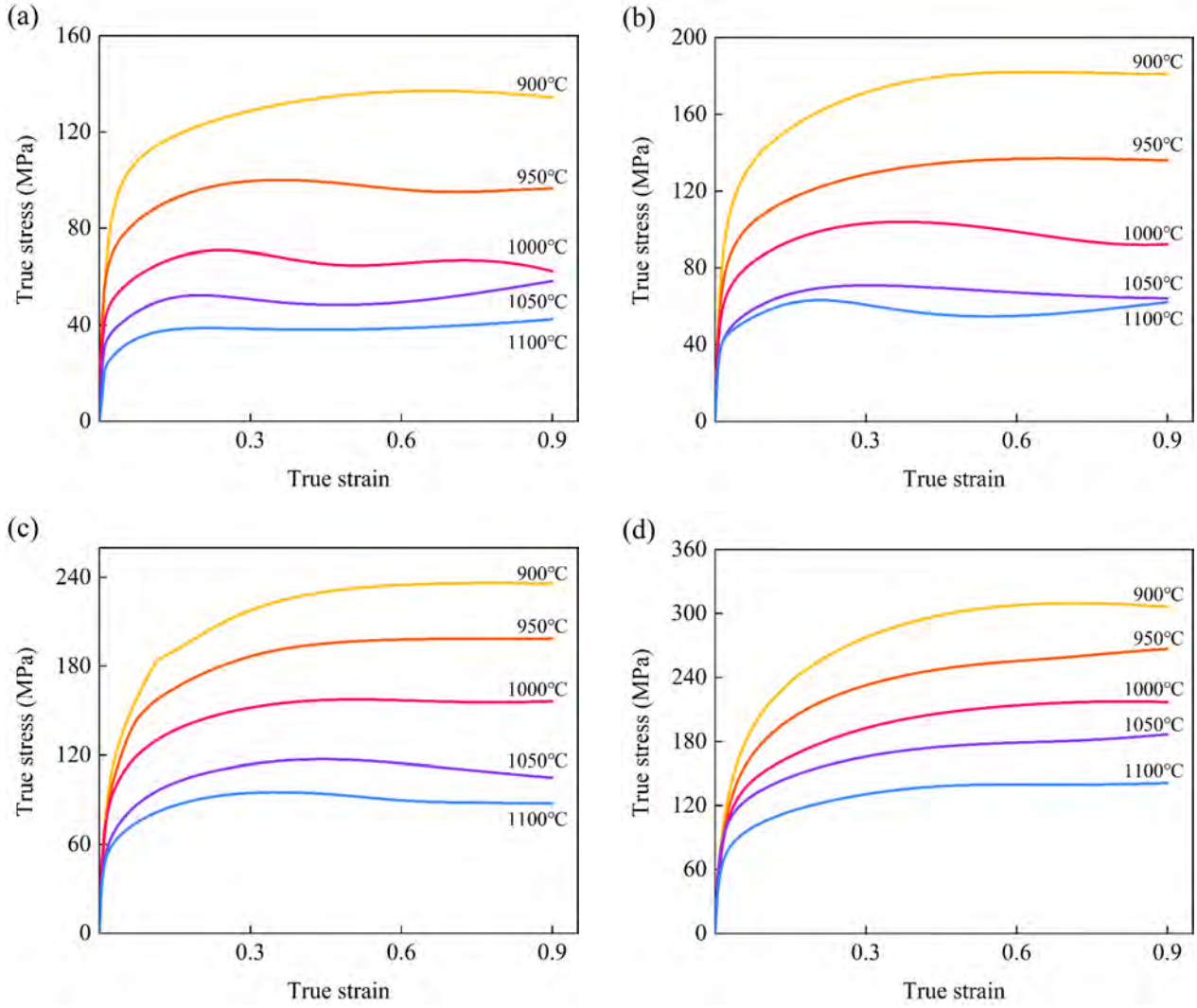

Fig. 3. True stress-strain curves at constant deformation temperature and constant strain rates of (a) $0.001s^{-1}$, (b) $0.01s^{-1}$, (c) $0.1s^{-1}$, (d) $1s^{-1}$.

3.1.2. Strain rate transient variation state

Fig. 4 depicts the flow stress curves of the samples deformed at 1000°C with strain rate transient variation. The solid line is the strain rate transient variation flow stress curves, while the dashed line is the flow stress deformed under a constant strain rate. Fig. 4(a) illustrates that the flow stress increased quickly owing to the WH at a strain rate of $0.01s^{-1}$, then slowly decreased after achieving the maximum value. The flow stress curves were the same with the constant state at the first deformation stage before a strain of 0.4. However, the flow stress increased again at a strain of 0.4. Following an intermediate transition mutation adjustment with a strain interval of 0.5, the stress gradually approached the constant deformation state with a strain rate of $0.1s^{-1}$. Since the dislocation multiplication induced by the increase in strain rate transient variation was unable to be equalized by DRX induced dislocation annihilation, this resulted in a sharp increase in stress. When the dislocation multiplication and annihilation were balanced again by

coordinated competitive timing, the flow stress gradually flattened out [27]. Fig. 4(a) also shows that from the onset of the dynamic increase (a strain of 0.4) to the end of compression (a strain of 0.9), there was sufficient time for WH and DS to coordinate competitive timing to reach equilibrium (a strain of 0.5). As a result, the stress was near the constant strain rate state at the end of deformation with the strain rate dynamic increase from $0.01s^{-1}$ to $0.1s^{-1}$. Notably, the stress was slightly lower than the constant strain rate deformation state. This is attribute to the distortion energy stored before the transient variation facilitated the development of DRX. In particular, it was also demonstrated that the critical strain for the occurrence of DRX at a constant strain rate was larger than that in the strain rate dynamic increase state.

Fig. 4(b) shows that the flow stress curves were the same at the first deformation stage before a strain of 0.4. The stress decreased rapidly and gradually approached a constant deformation state after an intermediate transition mutation adjustment with a strain interval of 0.1. It is noteworthy that the stress decreased rapidly after the strain rate dynamic decreased. Since the DRX is more likely to occur at a lower strain rate, the increasing DS effect is strengthened as the deformation proceeds. Furthermore, the thermal stress decreased with decreasing strain rate. The accumulated stored distortion energy was larger at $0.1s^{-1}$ initial high strain rate than that at $0.01s^{-1}$ constant strain rate. It was fully released after the dynamic change of strain rate, which significantly promoted the DS of the specimen, leading to a rapid reduction of flow stress. Some studies have also discovered that network dislocation density has a crucial impact on the flow stress evolution of SFE materials, resulting in a faster adaptation of the substructure to new deformation conditions, and rapidly reaching constant strain rate levels during dynamic change of strain rate [4]. However, this paper does not exhibit an abrupt decrease or sharp jump in flow stress during the dynamic decrease of strain rate reported in the literature [28]. As there was no unloading and reloading shift process during the strain rate transition mutation of the equipment used in this paper.

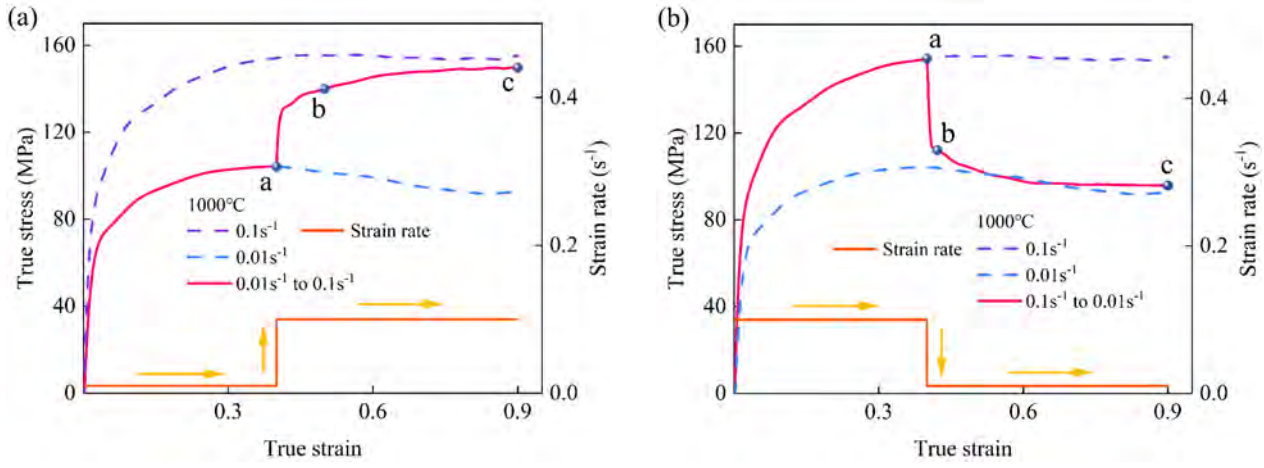

Fig. 4. True stress-strain curves at constant deformation temperature and transient strain rates of (a) $0.01s^{-1}$ to $0.1s^{-1}$, (b) $0.1s^{-1}$ to $0.01s^{-1}$.

3.1.3. Deformation temperature transient variation state

Fig. 5 shows the flow stress curves of specimens deformed to various strains at a strain rate of 0.01 s^{-1} with temperature transient variation. Fig. 5(a) displays that the stress gradually decreasing at a strain of 0.4 before the deformation temperature dynamic increases, which gradually flattened out after reaching a strain of 0.5. This is because the transient variation temperature changed at a 10°C/s state, and the increase from 1000°C to 1100°C required completion in the strain 0.1 interval. The flow stress after the deformation temperature dynamic increase was lower than that at a stable deformation temperature of 1100°C. This is explained by the dislocation motion before the deformation temperature transient variation contributes to the DRX behavior. With the deformation temperature dynamic increasing, the dislocation motion ability was further enhanced. The thermal activation energy increased, which promoted the GB migration ability, and the DRX softening ability was further strengthened, providing a stronger

softening effect during the deformation temperature dynamic increase.

Fig. 5(b) depicts the flow stress increased rapidly with the temperature lowered at a strain of 0.4 and increased slowly after reaching the strain of 0.5. The same is the case for the deformation temperature dynamic decrease, which was also completed in the strain 0.1 interval. The DS behavior was stronger due to the higher deformation temperature in the first stage (1100℃) at a strain of 0.4, which reached the steady stress stage. With the deformation temperature dynamic decreasing, the dislocation motion gradually decreased. The thermal activation energy decreased, which weakens the DRX behavior. The WH increased continuously, leading to a dramatic increase in flow stress in the transition zone. When the deformation temperature dynamic decreased to 1000℃, the flow stress slowly increased and continuously approached the constant deformation temperature state of 1000℃. This indicates that the WH and DS require a longer strain interval to reach a new equilibrium state under the deformation temperature dynamic decrease state. On the other hand, it is also possible that the presence of friction during the experimental process lead to an increase in flow stress after the temperature dynamic decreased. It is worth noting that comparing the strain rate with the deformation temperature variation shows that the flow stress after the transient variation is not completely consistent with the constant deformation state, which may also be related to the microscopic substructural changes during the transient variation deformation state.

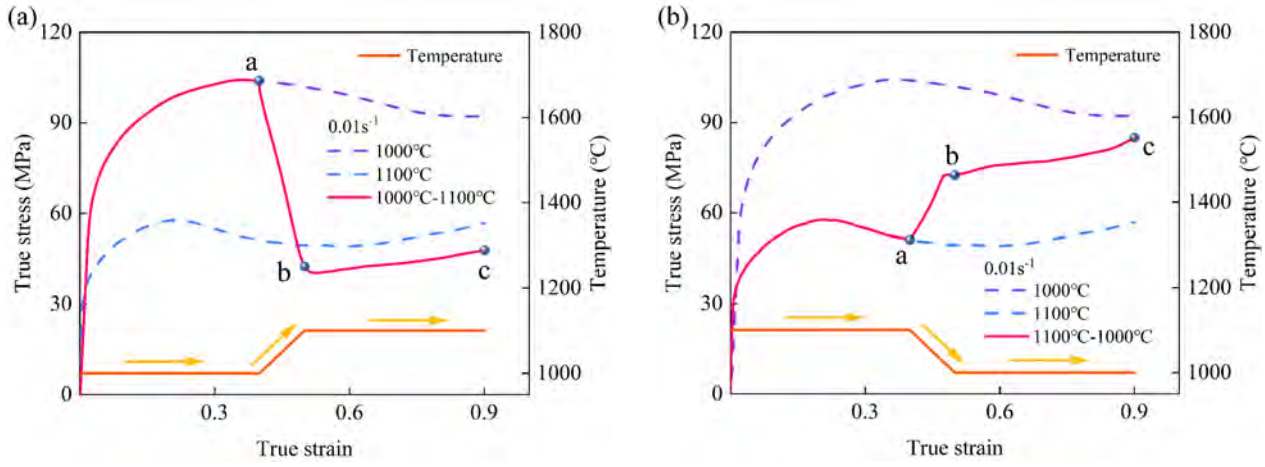

Fig. 5. True stress-strain curves at constant strain rate and transient deformation temperatures of (a) 1000℃ to 1100℃, (b) 1100℃ to 1000℃.

3.2. Kinetics analysis for constant deformation state

3.2.1. Critical state for dynamic recrystallization

Normally, the DRX critical strain is obtained using the following two methods: metallographic observation of the quenched specimen microstructure and the mathematical deduction of the flow stress curves [29, 30]. The Jonas and Mirzadeh methodology was applied to calculate the key factors, as expressed in Eq. (1) [31-33]. Accordingly, the DRX critical values can be obtained at different deformation states.

$$\begin{cases} \theta = \frac{\partial \sigma}{\partial \varepsilon} \\ \theta = a_1\sigma^3 + a_2\sigma^2 + a_3\sigma + a_4 \end{cases} \tag{1}$$

where a_1, a_2, a_3, and a_4 are values at a constant deformation state. σ and ε are stress and strain, respectively. θ is the WH rate, which can be used to determine the DRX threshold. When $\partial^2\theta/\partial\sigma^2 = 0$, the critical stress σ_c can be calculated.

The critical stress σ_c, critical strain ε_c, peak stress σ_p, and peak strain ε_p under constant deformation states can be obtained through mathematical analysis, as illustrated in Fig. 6. The critical and peak characteristics dropped with the decrease in strain rate and the increase of deformation temperature. This pattern reinforces the theory that low strain rates and high deformation temperatures enhance DRX behavior. Thus, the macroscopic flow stress exhibited

the above variation process. Fig. 7 depicts the link between the key parameters, i.e., $\sigma_c = 0.901\sigma_p$ and $\varepsilon_c = 0.352\varepsilon_p$.

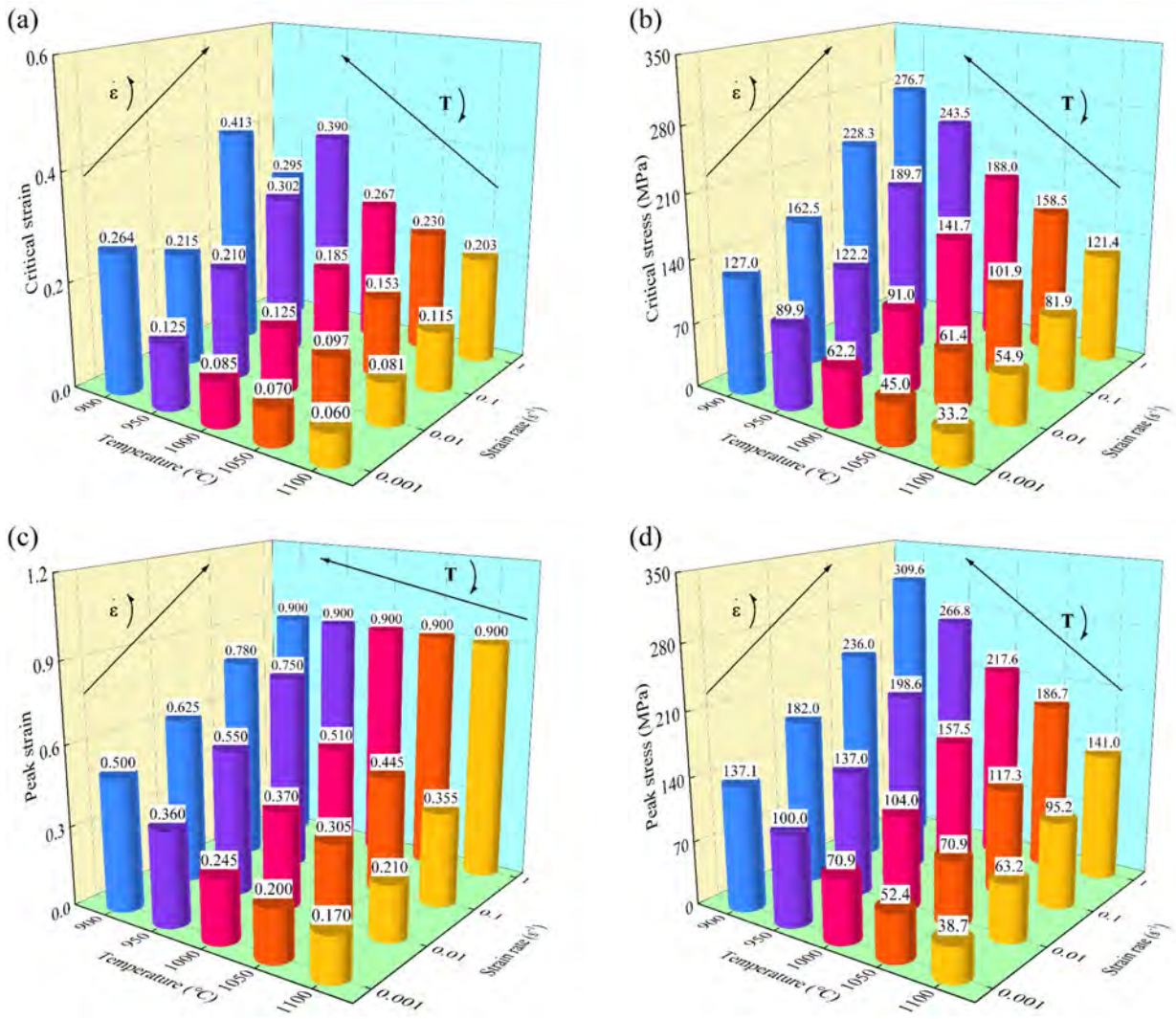

Fig. 6. Relationship between deformation temperature and strain rate versus state parameters of (a) ε_c, (b) σ_c, (c) ε_p, (d) σ_p under constant deformation conditions.

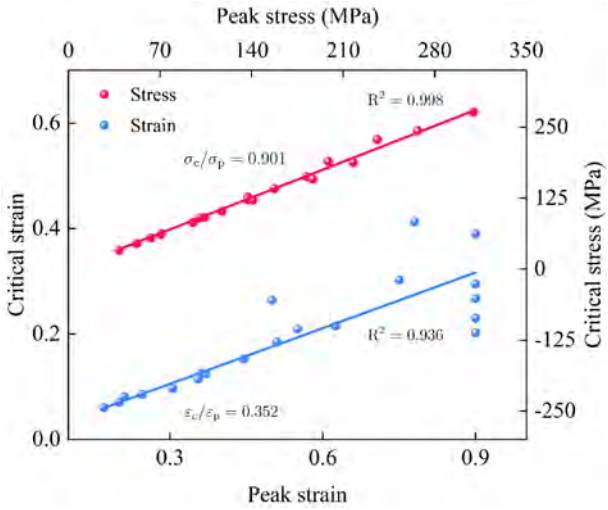

Fig. 7. Relationship between critical strain versus peak strain, and critical stress versus peak stress.

3.2.2. Arrhenius constitutive model

This work applied Sellars hyperbolic sin Arrhenius model to develop the coupling correlation between

temperature, stress, and strain rate [34-36], as shown in Eq. (2).

$$\dot{\varepsilon} = \begin{cases} A_1\sigma^{n_1}\exp\left(-\frac{Q}{RT}\right)(\alpha\sigma < 0.8, low\ stress\ level) \\ A_2\exp(\beta\sigma)\exp\left(-\frac{Q}{RT}\right)(\alpha\sigma > 1.2, high\ stress\ level) \\ A[sinh(\alpha\sigma)]^n\exp\left(-\frac{Q}{RT}\right)(all\ condition) \end{cases} \quad (2)$$

where A_1, A_2, A, n_1, n, β are material coefficients. α is the stress compensation coefficient ($\alpha \approx \beta/n_1$), which works to keep a linear relationship between $\ln\dot{\varepsilon}$ and $ln[sinh(\alpha\sigma)]$ within the deformation temperature. $\dot{\varepsilon}$ is the strain rate. Q is the hot deformation activation energy (kJ/mol). R is the gas constant (8.314 J/mol). T is the deformation temperature (K). σ is replaced by peak stress σ_p. Some studies emphasized the importance of peak stress σ_p in the actual production of steels [37]. The link between strain rate and deformation temperature is illustrated in Eq. (3) [38].

$$Z = \dot{\varepsilon}\exp\left(\frac{Q}{RT}\right) = A[sinh(\alpha\sigma)]^n \quad (3)$$

The physical meaning of the Zener–Hollomon factor is a dimensionless factor of strain rate based on temperature compensation. Using the logarithms on each side of Eq. (2) and linearly fitting $ln\dot{\varepsilon}$ and $ln\,\sigma_p$, $ln\dot{\varepsilon}$ and σ_p. The average value of the slopes of n_1 and β were obtained, respectively. Thus, α can be calculated as 0.0075. Subsequently, through the linear fitting of $ln\,\dot{\varepsilon}$ and $ln[sinh(\alpha\sigma_p)]$, $ln[sinh(\alpha\sigma_p)]$ and $1/T$. The average values of the slopes were n and Q, which is 4.626 and 425.106 kJ/mol, respectively. Thus, A value can be determined as 4.73×10^{15}. In this study, the value of n was 4.626, revealing that the glide and climb of dislocations in the climb regulated the regime [39]. The samples' chemical composition, which is related to higher solute levels, was consistent with the hot deformation activation energy Q that was determined [40]. Finally, the following equation may be used to express Eq. (2) and (3).

$$\dot{\varepsilon} = 4.73\times10^{15}[sinh(0.0075\sigma)]^{4.626}\exp\left(-\frac{425106}{RT}\right) \quad (4)$$

$$Z = \dot{\varepsilon}\exp\left(\frac{425106}{RT}\right) = 4.73\times10^{15}[sinh(0.0075\sigma)]^{4.626} \quad (5)$$

3.2.3. kinetic model of DRX

There are several methodologies to establish the DRX kinetics model [12, 41-43]. The DRX volume fraction in this work was evaluated using the method considering the DRV effect [44]. As shown in Eq. (6). The above section indicates that DRX happens at the critical strain. However, there are some studies in the construction of kinetic models that substitute the saturation stress σ_{sat} for peak stress σ_p [45-47]. The gap between σ_{sat} and σ_{ss} was utilized to determine the DRX volume fraction.

$$X_{\mathrm{DRX}} = \frac{\sigma_{DRV}-\sigma}{\sigma_{sat}-\sigma_{ss}} \quad (6)$$

where X_{DRX} is the DRX volume fraction calculated based on the experimental data (flow stress curves). σ_{DRV} is the DRV stress. σ_{sat} and σ_{ss} is the saturation stress and steady stress, respectively. σ and σ_{ss} can be determined directly from the flow stress curves, and σ_{DRV} can be estimated based on the Eq. (7).

$$\sigma_{DRV} = \sqrt{\sigma_{sat}^2 - (\sigma_{sat}^2 - \sigma_i^2)\exp(-r\varepsilon)} \quad (7)$$

where σ_i denotes the stress before the critical stress. r is the DRV factor. Since only DRV and WH occurred before DRX, Eq. (7) was derived as shown in Eq (8), then the r value could be calculated.

$$r\varepsilon = ln\left(\frac{\sigma_{sat}^2-\sigma_i^2}{\sigma_{sat}^2-\sigma_{DRV}^2}\right) \quad (8)$$

The DRX volume fraction can be determined using the aforementioned methodology according to experimental data. The Avrami formula was used to create the DRX prediction kinetic model, as shown in Eq. (9) [33].

$$X_{\mathrm{DRX}} = 1 - \exp\left(-b\left(\frac{\varepsilon-\varepsilon_c}{\varepsilon_p}\right)^k\right) \tag{9}$$

where b and k are factors linked to the element composition and deformation states of the samples, respectively. Eq. (6) and (9) were integrated to obtain the average values of the slope and intercept, for which b and k values were 1.315 and 2.321, respectively. The developed DRX kinetic model is illustrated in Eq. (10).

$$X_{\mathrm{DRX}} = 1 - \exp\left(-1.315\left(\frac{\varepsilon-\varepsilon_c}{\varepsilon_p}\right)^{2.321}\right) \tag{10}$$

Fig. 8 compares experimental and predicted X_{DRX} values. The predicted and experimental values followed well under all deformation conditions. The X_{DRX} decreased with decreasing deformation temperature or increasing strain rate, shows that DRX is inhibited at a higher Z value. The above results also proved the findings obtained from the flow stress analysis, e.g., the flow stress reached a peak at a strain rate of 0.001s^{-1} and deformation temperature of 950°C, then decreased, indicating the strong softening effect of DRX. However, when the DRX did not occur sufficiently at a higher strain rate of 1s^{-1} and the same deformation temperature, the flow stress did not tend to decrease significantly.

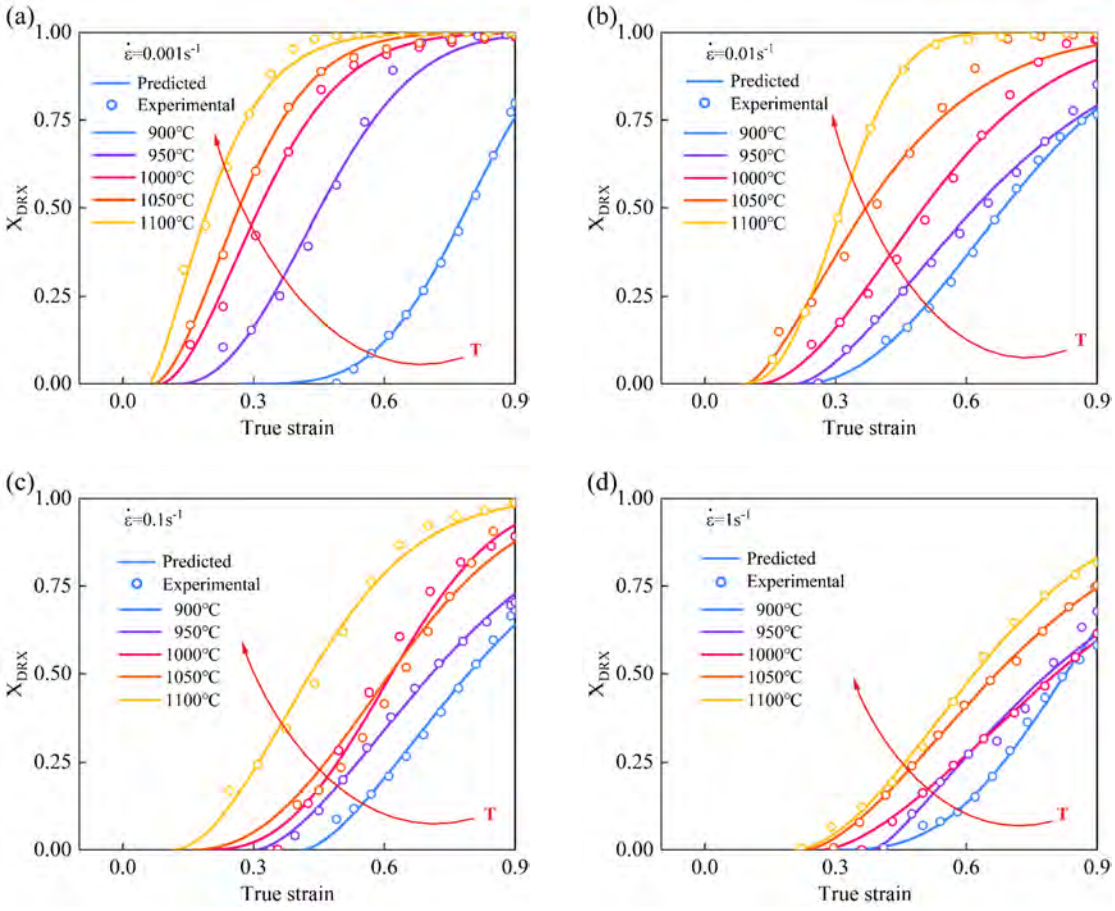

Fig. 8. Comparison of experimental and predicted values of DRX volume fraction at constant deformation temperature and constant strain rates of (a) 0.001s^{-1}, (b) 0.01s^{-1}, (c) 0.1s^{-1}, (d) 1s^{-1}.

Based on the DRX kinetic model, a flow stress prediction model considering the DRV effect is developed in this paper, as shown in Eq. (11).

$$\sigma = \begin{cases} \sigma_{DRV} = \sqrt{\sigma_{sat}^2 - (\sigma_{sat}^2 - \sigma_i^2)\, exp(-r\varepsilon)} & (\varepsilon < \varepsilon_C) \\ \sigma_{DRX} = \sigma_{DRV} - (\sigma_{sat} - \sigma_{ss})\left\{1 - \exp\left[-1.315\left(\frac{\varepsilon-\varepsilon_c}{\varepsilon_p}\right)^{2.321}\right]\right\} & (\varepsilon \geq \varepsilon_C) \end{cases} \tag{11}$$

Fig. 9 depicts the comparison of flow stress at a constant deformation state, from which it can be seen that the

experimental and predicted values match well during the deformation range, and the established model can be used to reveal the flow behavior of the experimental steel during high-temperature plastic deformation process.

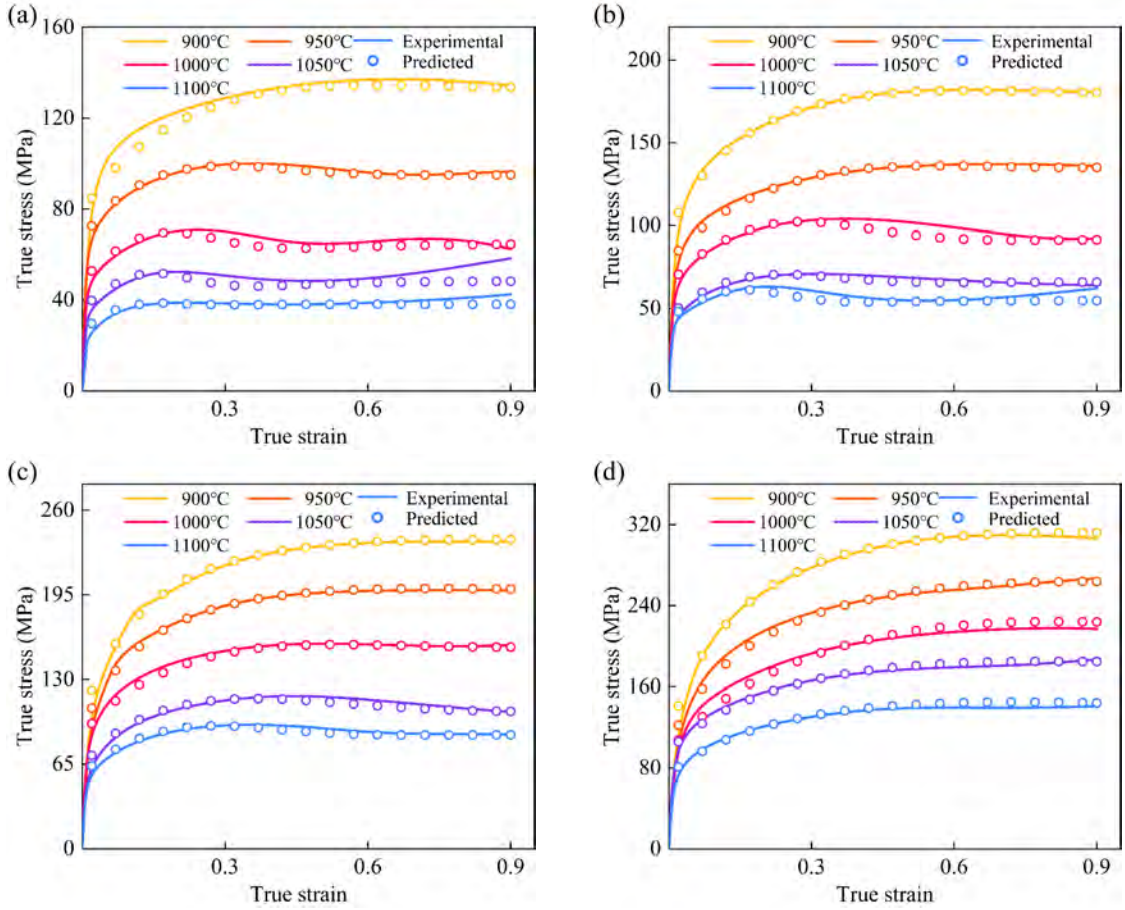

Fig. 9. Comparison of experimental and predicted values of true stress-strain curves at constant deformation temperature and constant strain rates of (a) 0.001s^{-1}, (b) 0.01s^{-1}, (c) 0.1s^{-1}, (d)1s^{-1}.

3.3. Kinetics analysis for transient deformation state

The analysis in the above section allows for predicting the flow stress and DRX volume fraction of the specimen under a constant deformation state. It is characterized by correlating the deformation temperature and strain rate with the flow stress. The total strain applied to the specimen can be expressed in two different types. Firstly, for the description of the work hardening at the beginning of plastic deformation. Secondly, the Avrami equation for the computation of DRX volume fraction [48]. However, the deficiency of this model is that it cannot update the transient variation of deformation temperature and strain rate, which is not applicable to describe the flow stress and DRX volume fraction of the specimen under the transient deformation state [49]. Therefore, it is necessary to develop a new constitutive model based on effective state parameters, which further reflects the flow stress independent of the applied total strain. Moreover, it can also describe the work hardening and softening process of the flow stress under a transient deformation state.

Based on the conventional constitutive model and DRX kinetic model established by Eqs. (2)-(11) for the constant deformation state. In this paper, the conventional model is extended by using numerical integration to implement the updating of strain rate and deformation temperature after each strain increment throughout the deformation schedule [50].

As derived from Eq. (11). if $\sigma_{DRV} < \sigma_c$, the flow stress of the material, σ is determined by σ_{DRV}. Otherwise, the flow stress and DRX volume fraction should be computed from the numerical integration of the following new differential equation here proposed:

$$\frac{d\sigma}{d\varepsilon}=\frac{r\left(\sigma_{sat}^2-\sigma_0^2\right)\exp(-r\varepsilon)}{\sqrt{\sigma_{sat}^2+\left(\sigma_0^2-\sigma_{sat}^2\right)\exp(-r\varepsilon)}}(\varepsilon<\varepsilon_c) \tag{12}$$

$$\frac{d\sigma}{d\varepsilon}=\frac{r\left(\sigma_{sat}^2-\sigma_0^2\right)\exp(-r\varepsilon)}{\sqrt{\sigma_{sat}^2+\left(\sigma_0^2-\sigma_{sat}^2\right)\exp(-r\varepsilon)}}-\frac{kt}{\varepsilon_p}(\sigma_{sat}-\sigma_{ss})\exp\left(-k\left(\frac{\varepsilon-\varepsilon_c}{\varepsilon_p}\right)^t\right)\left(-k\left(\frac{\varepsilon-\varepsilon_c}{\varepsilon_p}\right)^{t-1}\right)(\varepsilon\geq\varepsilon_c) \tag{13}$$

$$\frac{dX}{d\varepsilon}=\frac{kt}{\varepsilon_p}\exp\left(-k\left(\frac{\varepsilon-\varepsilon_c}{\varepsilon_p}\right)^t\right)\left(-k\left(\frac{\varepsilon-\varepsilon_c}{\varepsilon_p}\right)^{t-1}\right)(\varepsilon\geq\varepsilon_c) \tag{14}$$

It is assumed that the value of the constant n in Eq (2) come out as temperature independent [51]. The correspondence between ε_c, ε_p, σ_c, σ_p, σ_0, σ_{sat}, σ_{ss}, r and Z values is calculated using the form of Arrhenius power law, as shown in Fig. 10.

$$\varepsilon_c=\begin{cases}0.00021Z^{0.18058} & \ln Z<40\\ 0.01321Z^{0.07929} & \ln Z\geq 40\end{cases} \tag{15}$$

$$\varepsilon_p=\begin{cases}0.00073Z^{0.17518} & \ln Z<40\\ 0.59339Z^{0.0087} & \ln Z\geq 40\end{cases} \tag{16}$$

$$\sigma_c=\begin{cases}0.11868Z^{0.18488} & \ln Z<40\\ 2.27532Z^{0.10869} & \ln Z\geq 40\end{cases} \tag{17}$$

$$\sigma_p=\begin{cases}0.17909Z^{0.17695} & \ln Z<40\\ 4.22546Z^{0.09693} & \ln Z\geq 40\end{cases} \tag{18}$$

$$\sigma_0=\begin{cases}0.34196Z^{0.14621} & \ln Z<40\\ 15.4111Z^{0.04537} & \ln Z\geq 40\end{cases} \tag{19}$$

$$\sigma_{sat}=\begin{cases}0.29277Z^{0.16754} & \ln Z<40\\ 14.2437Z^{0.07055} & \ln Z\geq 40\end{cases} \tag{20}$$

$$\sigma_{ss}=\begin{cases}0.12379Z^{0.18763} & \ln Z<40\\ 3.46977Z^{0.10269} & \ln Z\geq 40\end{cases} \tag{21}$$

$$r=24.2515Z^{-0.04377} \tag{22}$$

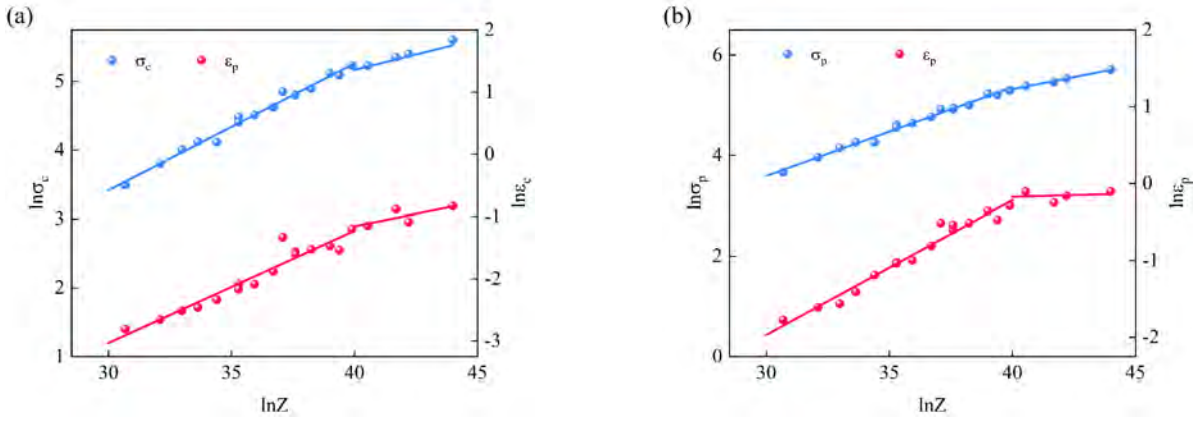

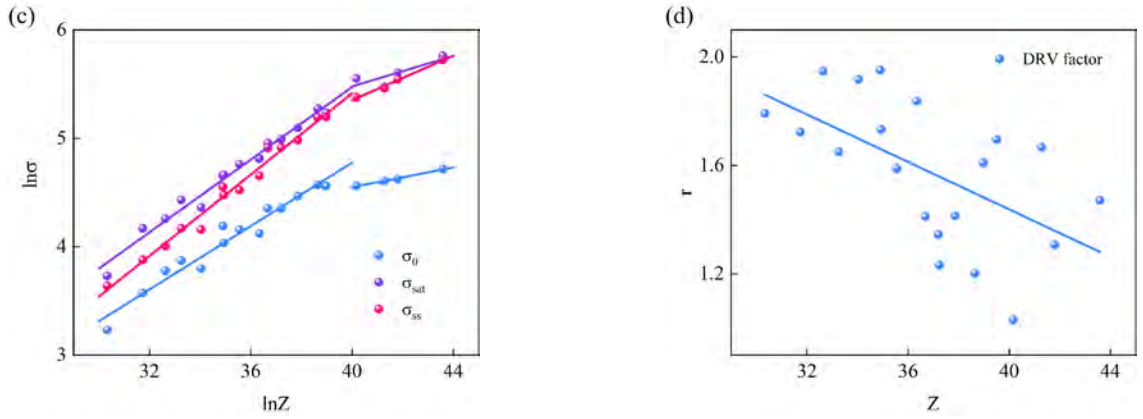

Fig. 10. Relationship between $\ln Z$ and state parameters of ε_c, ε_p, σ_c, σ_p, σ_0, σ_{sat}, σ_{ss}, r. (a) $\ln Z$ versus ε_c, σ_c, (b) $\ln Z$ versus ε_p, σ_p, (c) $\ln Z$ versus ε_0, σ_{sat}, σ_{ss}, (d) $\ln Z$ versus r.

Taking the state variables into Eq. (12) and (13) allows the prediction of flow stress under a transient deformation state. Fig. 11(a) and (b) show the predicted flow stress curves of the specimen deformed at 1000℃ with strain rate transient variation. Fig. 11(c) and (d) show the predicted flow stress curves of the specimen deformed to various strains at a strain rate of 0.01 s^{-1} with temperature transient variation. It can be seen from Fig. 11 that the strain rate or deformation temperature undergoes a transient mutation when the strain reached 0.4. The flow stress changes instantaneously to the second-stage flow stress at the mutation site, but does not approach the second-stage flow stress as slowly as the experiment, which may be related to the relationship between the state parameters and Z value. It is worth noting that the buckling behavior of the flow stress cannot be predicted under a transient deformation state, which may be related to the experimental equipment and the grain size of the material [27].

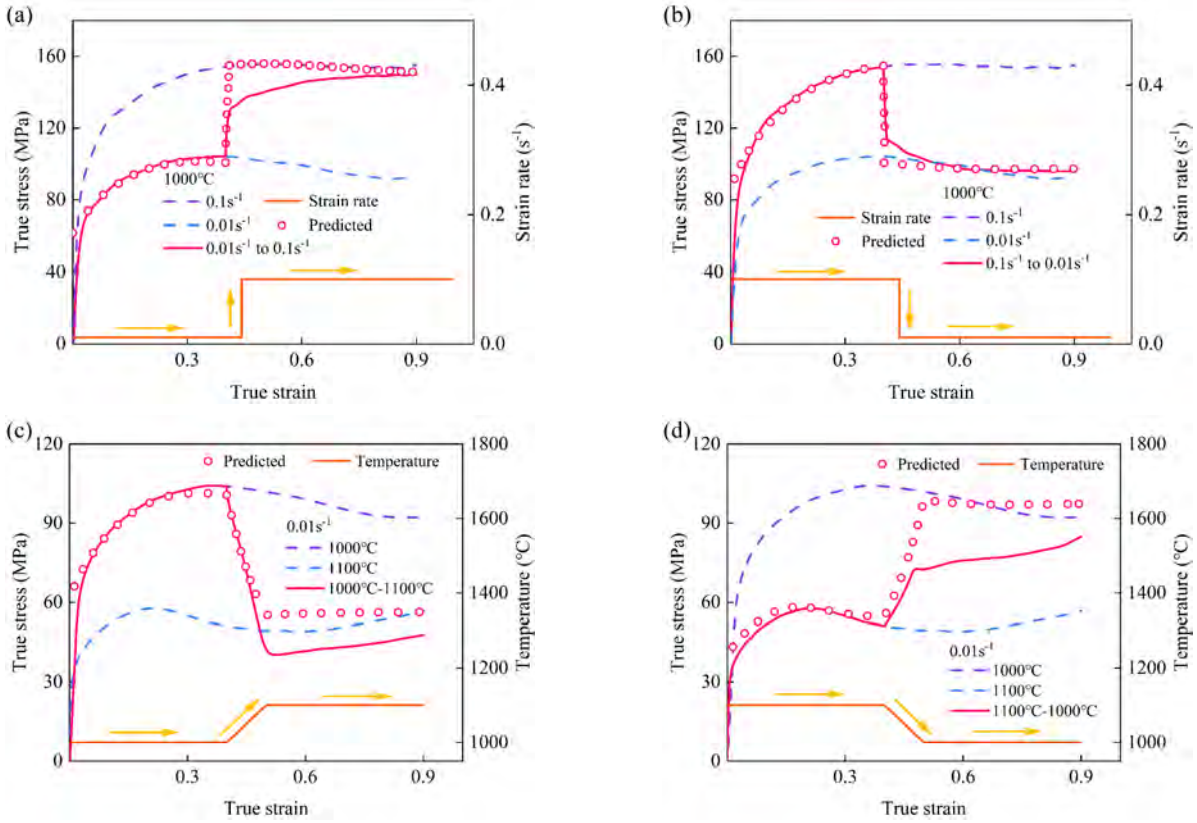

Fig. 11. Comparison of experimental and predicted values of true stress-strain curves at constant deformation temperature and transient strain rates of (a) 0.01s^{-1} to 0.1s^{-1}, (b) 0.1s^{-1} to 0.01s^{-1}. Comparison of experimental and predicted values of true stress-strain curves at constant strain rate and transient deformation temperatures of (c)

1000℃ to 1100℃, (d) 1100℃ to 1000℃.

The prediction of the DRX volume fraction of the specimen under a transient deformation state can be achieved by implementing the state variables into Eq. (14), as shown in Fig. 12. It can be seen from Fig. 12 that the DRX volume fraction changes with transient variations of the deformation parameters, e.g., Fig. 12 shows that the lower strain rate in the first stage facilitates the occurrence of DRX in the strain rate transient mutation state. With the transient increase in strain rate, the DRX behavior is inhibited and the velocity of the DRX volume fraction is slow. Although a fully recrystallized state occurred in both deformation temperature transient mutation states, the higher deformation temperature in the first stage can promote the DRX behavior. It is not possible to predict the variation of DRX volume fraction with time (strain) for transient variations, this reason can also derive from the above analysis.

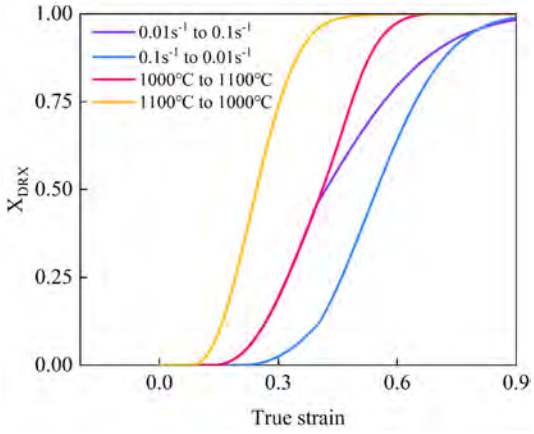

Fig. 12. Comparison of experimental and predicted values of DRX volume fraction at transient deformation temperatures of 1000℃ to 1100℃, 1100℃ to 1000℃, and transient strain rates of $0.01s^{-1}$ to $0.1s^{-1}$, (b) $0.1s^{-1}$ to $0.01s^{-1}$.

3.4. Assessment of hot workability

3.4.1. Power dissipation efficiency and instability factor

Following the dynamic material model theory [6], the total input energy can be expressed as Eq. (23)

$$\begin{cases} P = \sigma\dot{\varepsilon} = G + J \\ G = \int_0^{\dot{\varepsilon}} \sigma d\dot{\varepsilon} \\ J = \int_0^{\sigma} \dot{\varepsilon} d\sigma \end{cases} \tag{23}$$

where P is the input energy. G is the energy related to deformation, which is mostly dissipated by heat during deformation and stored as distortion energy within the deformed material. J is the power dissipated by microstructural development, such as DRV or DRX, during hot deformation. The proportion of G and J in P is described using the strain rate sensitivity index m, as expressed in Eq. (24) [52].

$$m = \frac{\partial log\sigma}{\partial log\dot{\varepsilon}} \tag{24}$$

It is noteworthy that the value of m varied nonlinearly when the deformation factor changed [53]. The power dissipation potential of the sample was assessed by introducing a dimensionless factor of PDE η [54], as expressed in Eq. (25).

$$\eta = \frac{2m}{m+1} \tag{25}$$

The PDE allowed an initial assessment of the influence of deformation states on the microstructure development of alloys such as DRV, DRX, microcracking, macroscopic shear band, local flow, and superplastic deformation [55, 56]. Nevertheless, a higher PDE can be acquired in certain conditions, such as edge cracks and pore instabilities. As a result, the PDE value η is insufficient to define the optimal hot workability region, which should be combined with

an instability criterion, as shown in Eq. (26) [57].

$$\xi(\dot{\varepsilon}) = \frac{\partial log\frac{m}{m+1}}{\partial log\dot{\varepsilon}} + m \tag{26}$$

$\xi(\dot{\varepsilon})$ is a dimensionless instability factor, and the flow instability occurs when $\xi(\dot{\varepsilon}) < 0$. The types of instability include local flow, the adiabatic shear band (ASB) and wedge cracking.

3.4.2. 3D power dissipation map and 3D instability map

The combined logarithm of strain rate and deformation temperature on the x and y axis, respectively, and PDE contour maps at different strains on the z-axis. 3D PDE maps and instability maps can be created, as depicted in Fig. 13(a). The maximum PDE value was 43.6%, corresponding to a strain of 0.4, strain rate of 0.001s^{-1} and a deformation temperature of 1020℃. At strains of 0.2 and 0.6, PDE decreased with the decreasing strain rate and deformation temperature. A higher PDE value can be obtained at a high strain rate and deformation temperature. The maximum value of PDE gradually reduced with increasing strain, but the maximum value of PDE remained in the higher strain rate condition.

Fig. 13(b) depicts the 3D instability maps of the samples deformed to various strains under different parameters. The green color on the map reflects the stable region, while the yellow color reflects the instability region. It had a region of instability throughout the strain range. The instability area had a higher deformation temperature and strain rate at a strain of 0.2. The instability area shifts toward lower temperatures with increasing strain.

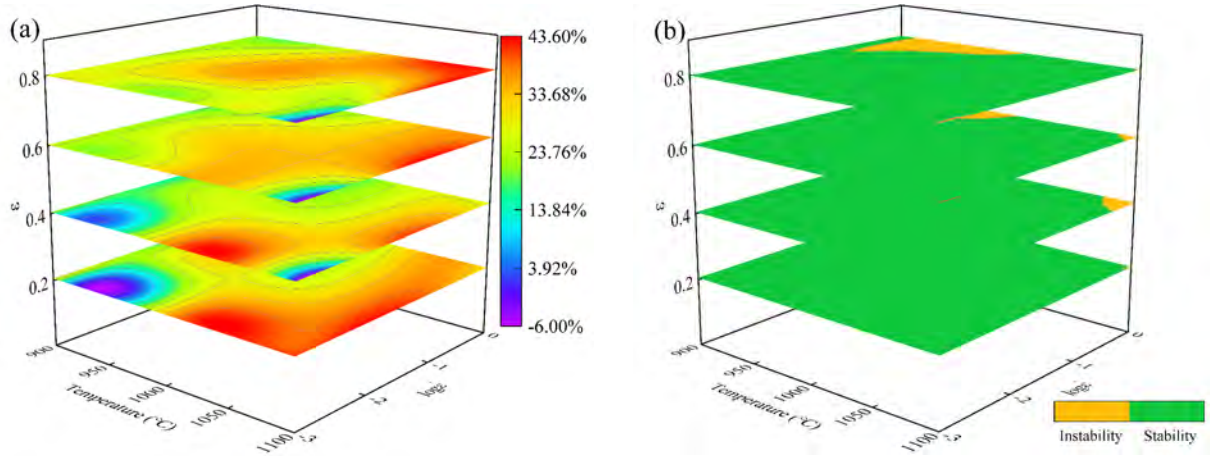

Fig. 13. The variation of: (a) power dissipation efficiency at the strain rates of 0.001-1s^{-1}, deformation temperatures of 900-1100 ℃, and true strains of 0.2-0.8, (b) instability region at the strain rates of 0.001-1s^{-1}, deformation temperatures of 900-1100 ℃, and true strains of 0.2-0.8.

3.4.3. Hot processing map and microstructure characterization

Fig. 14 illustrates the HPM of the samples deformed under variable deformation parameters. The instability zone is shown by the shaded area and the green dotted lines. When the strain was 0.2, the maximum PDE value was located at higher strain rates and deformation temperatures, whereas the instability area appeared in the opposite direction. The instability region began to move toward the higher deformation temperature with the increase of strain from 0.2 to 0.4. When the strain was 0.6 and 0.8, the instability region varied less with the strain increase and was mostly localized at the range of 1080℃ to1100℃ and 0.21s^{-1} to 1s^{-1}. Fig. 14 shows that instability tended to occur when the PDE was lower. Specifically, instability occurred when the PDE was lower than 28%, implying that the PDE of 28% may be a critical value that leads to the instability occur of the material.

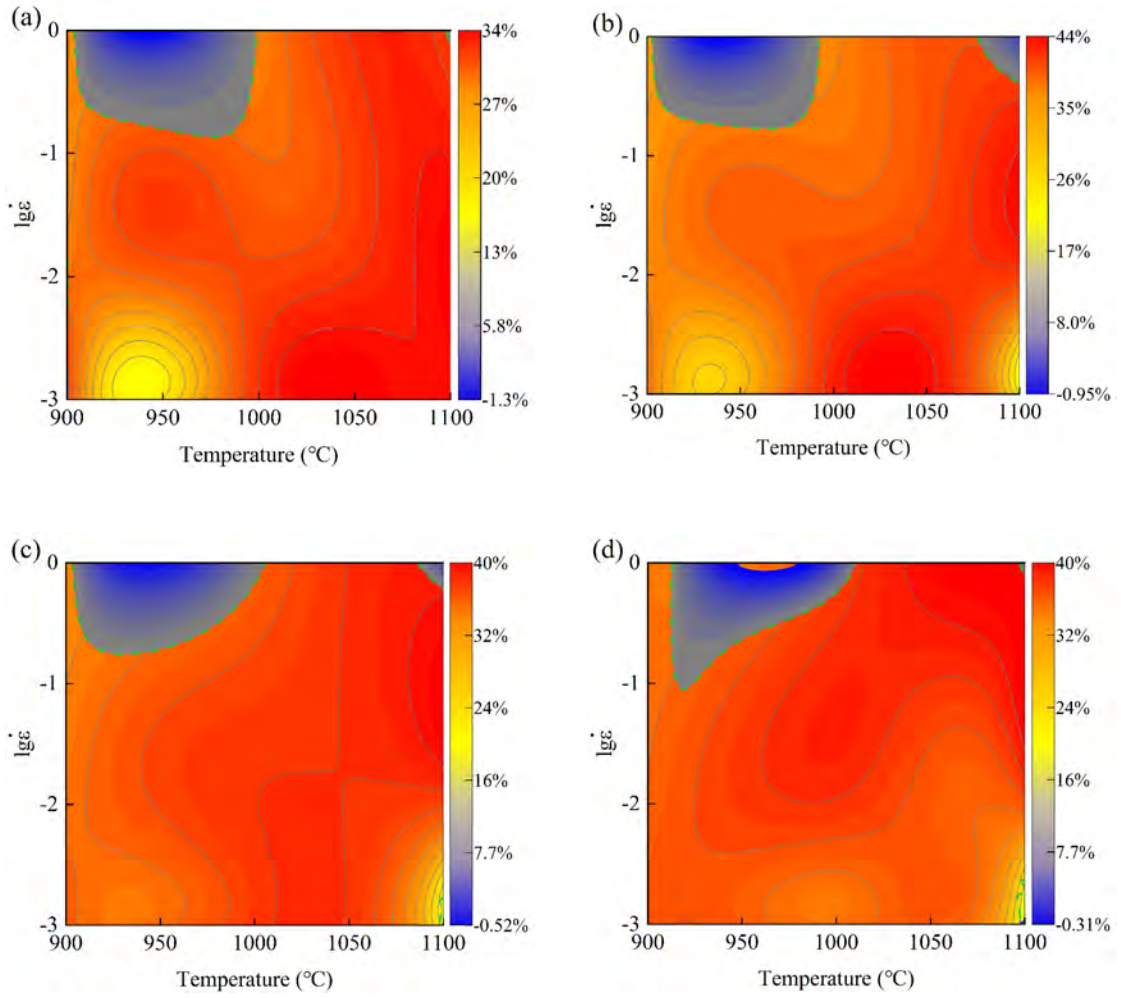

Fig. 14. Hot processing maps of 316L at the strain rates of 0.001-1s^{-1}, deformation temperatures of 900-1100 °C, and true strains of (a) 0.2, (b) 0.4, (c) 0.6, (d) 0.8. The shaded region and the green dotted lines represent the instability region.

The microstructure development in response to the current deformation parameters is indicated by the PDE and instability area in the HPM [58-60]. To evaluate the accuracy of the developed HPM, there is a need to further investigate the microstructure evolution under specific process parameters [61]. In this paper, four areas (including stable and instability areas) were chosen from the HPM, and the corresponding samples were analyzed. The selected area was deformed to a strain of 0.9 under all constant deformation states, as depicted in Fig. 15. Area A is the instability region deformed at 913°C-1008°C and 0.16s^{-1}-1s^{-1}. The PDE value was 17% - 28%. The deformation state exhibited local flow behavior. The shear direction and compression direction axes formed a 30° angle. Based on their specific location in the ASB, all grains in the ASB area underwent various degrees of deformation. These grains experienced the greatest deformations in the center of the ASB line. Furthermore, there was a small and inhomogeneous transition zone between the ASB center and the matrix. The steel was in a non-uniform deformation state with low hot workability. This combination of working parameters must be avoided during thermomechanical processing. Area B is the stable region deformed at 1050°C-1090°C and 0.1s^{-1}-1s^{-1}. The PDE was 38% - 43%. The DRX volume fraction and the PDE increased with increasing deformation temperature. This may be due to the effect of the higher strain rate state promoting DRX behavior coupled with the effect of higher deformation temperature and heat generated during plastic deformation. Fig. 15 shows that the microstructure underwent a significant DRX, with the GB bulging to form recrystallization nuclei. The original deformed grains were surrounded by the newly generated DRX grains. Furthermore, the diffusion and migration of dislocations were strengthened, and the GB migration duration was

shortened at a high deformation temperature and strain rate. This state promotes DRX nucleation. Area C is the instability region deformed at 1050℃-1100℃ and $0.003s^{-1}$-$0.01s^{-1}$. This area was undergone a higher deformation temperature and lower strain rate with a PDE value of 10% - 20%. The instability factor was below zero. The microstructure was coarse and non-uniformly distributed in comparison to area B, which may be destabilized during hot deformation. Area D is the stable region deformed at 900℃-930℃ and $0.001s^{-1}$-$0.01s^{-1}$. The PDE in this area was 22% - 26%. Most of the microstructure in area D was made up of deformed grains. The primary mechanism of microstructure development is DRV, with a small fraction of DRX grains and relatively few interior defects. It should be noted that in area D the deformation temperature and strain rate were lower, indicating that DRX at a lower temperature also needs to be accompanied by a lower deformation rate.

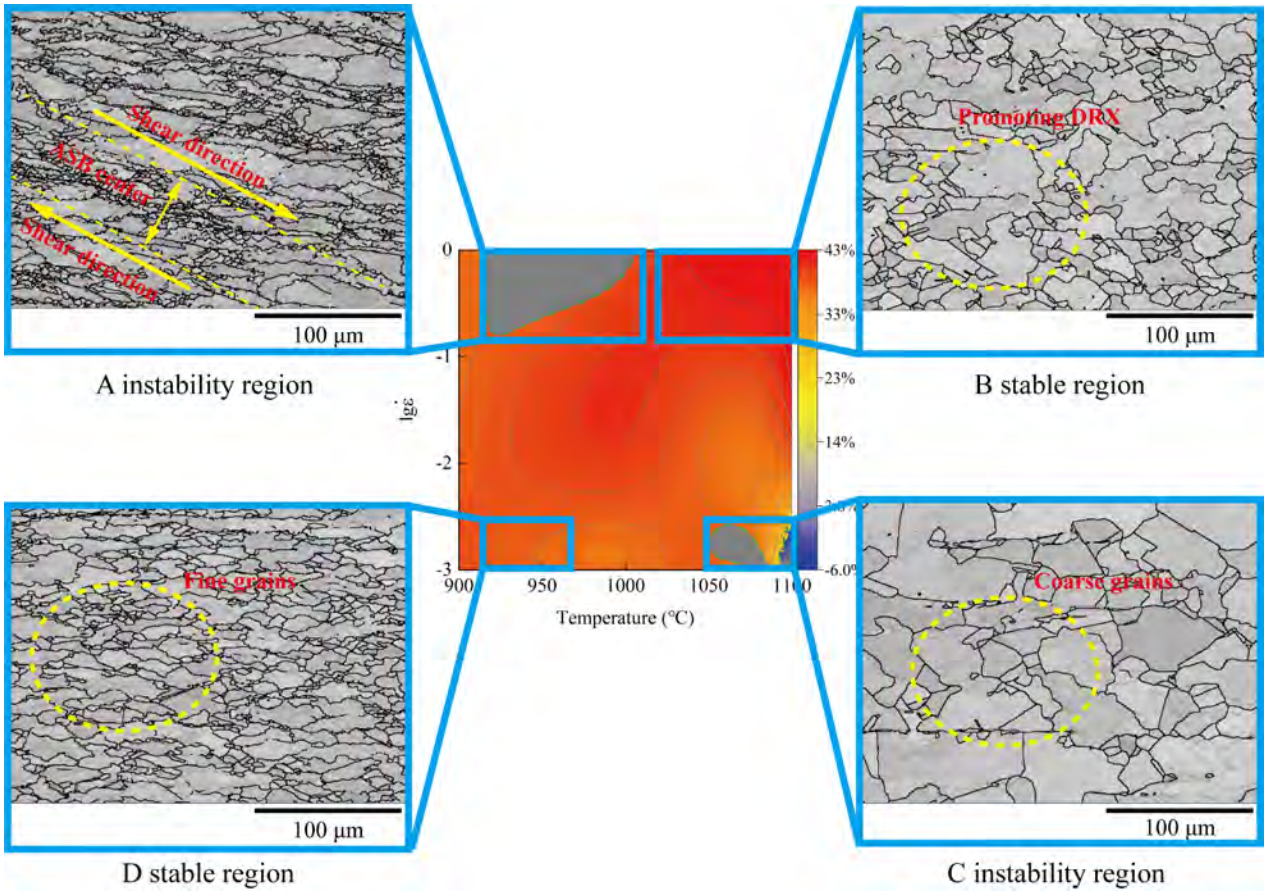

Fig. 15. Microstructure of different regions of the hot processing map at the strain rates of 0.001-$1s^{-1}$, deformation temperatures of 900-1100 ℃, and true strain of 0.9. The shaded region and the green dotted lines represent the instability region.

3.5 Microstructure in transient variation deformation state

3.5.1 Strain rate dynamic increase

Fig. 16(a) - (i) show the three characteristic sites a, b, and c of the flow stress curve marked in Fig. 4(a), which are used to study the microstructure development regulation mechanism before and after the strain rate dynamic increase. Fig. 16(a), (d) and (g) show that the LAGBs transformed into MAGBs, and HAGBs accelerated as the deformation proceeded. Many fine DRX grains can be seen to be defined partially by LAGBs and HAGBs. The appearance of incomplete HAGBs indicates the gradual transformation of the substructure towards general GB during deformation. Generally, the point to origin (cumulative) and point to point (local) misorientations along the GB or within the grain can trace the regulation mechanism of distortion energy. Especially when the cumulative misorientation is less than 15°, this represents the occurrence of substructure caused by dislocation motion, When the substructure is transformed into newly generated grains, the misorientation angle will exceed 15° [25]. Fig. 16(b), (e)

and (h) show the local misorientation (LocMis) map of the samples at the characteristic sites. Fig. 16(c), (f) and (i) show the local and cumulative misorientation angles along or within the grain. Fig. 16(b), (c) shows that the LocMis angle was low before the increase in strain rate. The cumulative misorientation angle along the GB or within the grain was less than 15°. This indicates that the deformation degree was low at a strain of 0.4, some of the grains exhibited nucleation through GB bulging. The recrystallized grains grew with the long-term migration of HAGBs, which is compatible with the nucleation mechanism of DDRX. When the strain rate transient variation jumped from $0.01s^{-1}$ to $0.1s^{-1}$, the LocMis angle gradually increased as depicted in Fig. 16(e), (f). The cumulative misorientation angle of the grain edge and interior exceeded 15°, which indicated that the material's internal dislocation movement is intense, and LAGBs at the edges or within the grain was transformed into MAGBs and HAGBs. This transformation is compatible with the nucleation mechanism of CDRX [62]. Moreover, the cumulative misorientation angle at GB was higher than that within the grain, revealing that DRX behavior is more likely to occur near the GB. When the sample deformed to the end after the strain rate dynamic increase, as shown in Fig. 16(h), (i), more recrystallized grains were formed and the newly generated recrystallized grains had a lower LocMis angle, replacing the deformed matrix grains gradually. The cumulative misorientation angle within the deformed grains was lower than 15°, and most areas of the edge cumulative misorientation angle were lower than 15°. This reveals that the stored distortion energy increases as deformation proceeds, which promotes DRX behavior and provides the motivation for dislocation rearrangement to prevent the development of the high intragranular misorientation gradient. Fig. 16 shows that the density and misorientations of the strain-induced substructure regulated the development of DRX in the interiors of the initial grains. The dislocations were rearranged to generate a microscopic substructure of LAGBs during deformation. Some grains appeared to be protruding and gradually changed from LAGBs to MAGBs and HAGBs with the jump in strain rate, new grains developed within the deformed grains. As a result, the recrystallization mechanism underwent a transformation from DDRX to CDRX during the strain rate dynamic increase, which differs from the constant deformation state [63, 64].

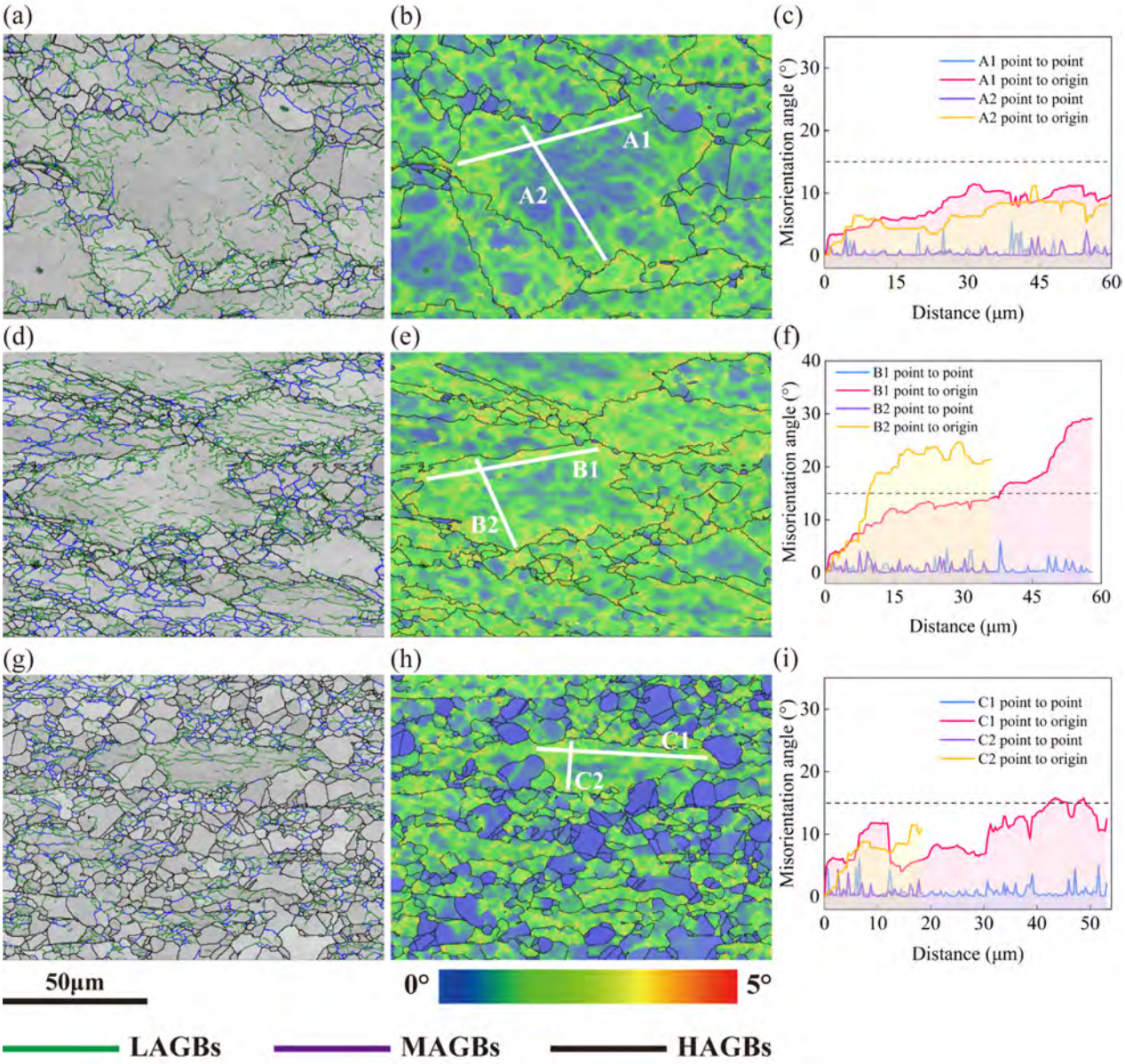

Fig. 16. Microstructure evolution at constant deformation temperature and strain rate dynamic increase from 0.01 s^{-1} to 0.1 s^{-1}. (a) Grain boundary map at strain of 0.4, (b) Local misorientation map of (a), (c) Changes in misorientation angle along the lines highlighted in (b), (d) Grain boundary map at strain of 0.5, (e) Local misorientation map of (d), (f) changes in misorientation angle along the lines highlighted in (e), (g) Grain boundary map at strain of 0.9, (h) Local misorientation map of (g), (i) Changes in misorientation angle along the lines highlighted in (h). There, A1, B1, C1 lines represent along the grain, A2, B2, C2 lines represent within the grain. The green, blue, and black lines represent LAGBs, MAGBs, HAGBs, respectively.

3.5.2 Strain rate dynamic decrease

Fig. 17 shows the microstructure at three characteristic sites from strain rate dynamic decrease to a, b and c in Fig. 4(b). Fig. 17(a), (d) and (g) show the GB map. More LAGBs and MAGBs appeared inside the grain before the strain rate dynamic decreased, as displayed in Fig. 17(a). The original deformed grains were transformed into the microscopic substructure and generated new recrystallized grains. The recrystallized grains without LAGBs and MAGBs inside grew as the strain rate dynamic decreased, as illustrated in Fig. 17(d) and (g). Fig. 17(b), (e), (h) show the LocMis map and Fig. 17(c), (f), (i) show the local and cumulative misorientation angle along the GB or within the grain. Fig. 17(b) and (c) illustrate that the cumulative misorientation angle along the GB and within most of the internal areas of the grains was higher than 15° at a strain of 0.4, indicating that the misorientation spanned a wide range from

the edge to the internal areas of the grains. Many LAGBs transformed into MAGBs and HAGBs, which corresponds to the characteristics of the CDRX mechanism. The LocMis angle changed alternately, indicating that the dislocation movement caused by the recovery process is intense at the moment. When the strain rate dynamic decreases to a strain of 0.5, as depicted in Fig. 17(e) and (f). The local and cumulative misorientation angle along or within the grain was lower than 15°, showing that the accumulated stored distortion energy before the transient variation was released after the strain rate dynamic decreased. The accumulated distortion energy and long-term migration of HAGBs were combined to enhance the DRX behavior. As a result, the volume fraction of DRX was higher at a strain of 0.5. The deformation reached its end at a decreased strain rate of $0.01s^{-1}$, as shown in Fig. 17(h) and (i). In most areas of the grains, the LocMis angle varied less, and the cumulative misorientation angle was less than 15°. Many recrystallized grains were generated by the long-term migration of HAGBs, and the dynamically recrystallized grains were nucleated by deformed GB bulging (nucleation mechanism of DDRX). There was less substructure inside the recrystallized grain, and the deformation period generated under a lower strain rate state was enough to enhance the dynamics participating in substructure development and dislocation rearrangement, preventing the establishment of the strong intragranular LocMis gradient. Thus, the DRX mechanism shifts from CDRX to DDRX during the strain rate dynamic decrease.

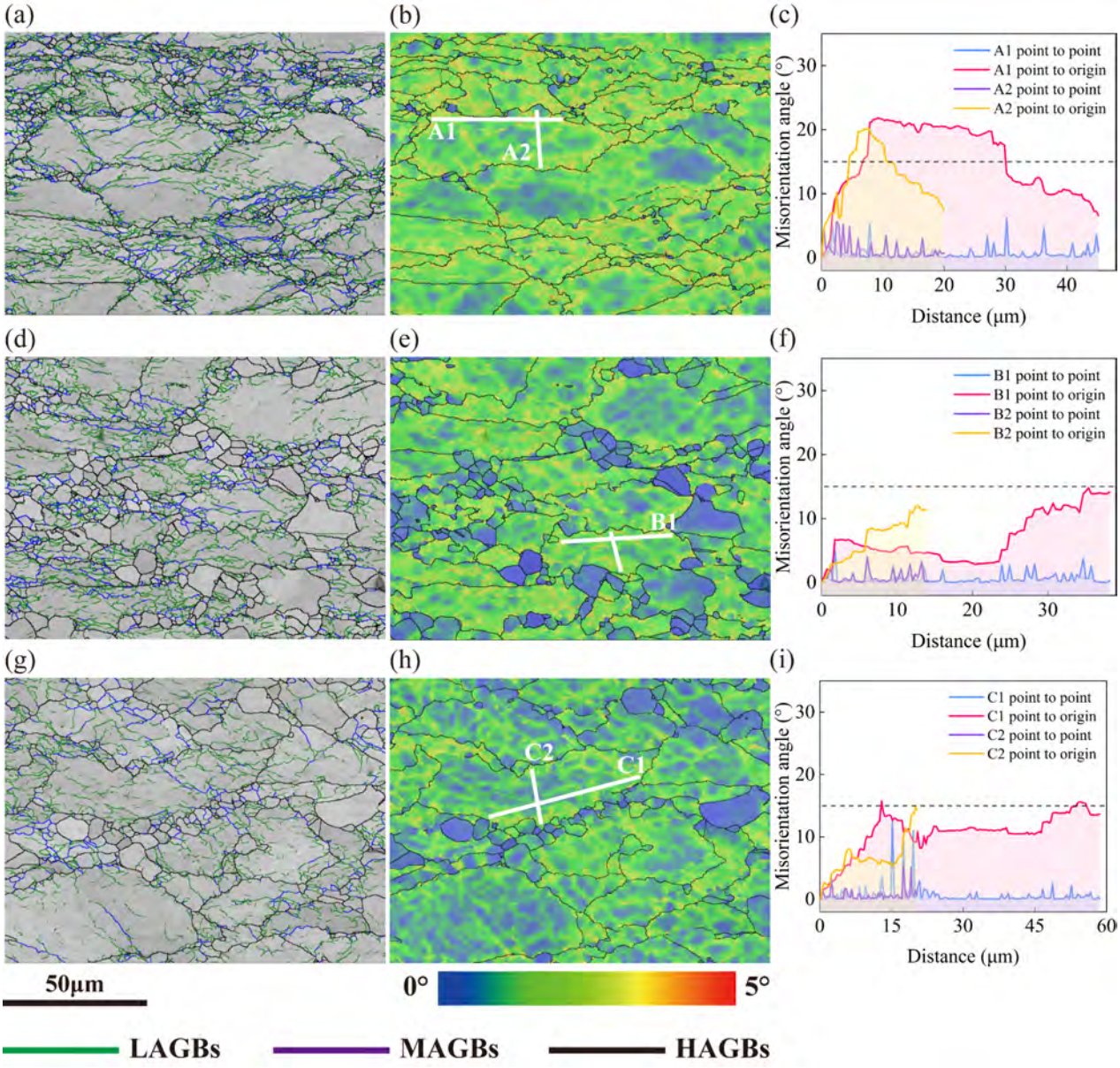

Fig. 17. Microstructure evolution at constant deformation temperature and strain rate dynamic decreased from 0.1 s^{-1} to 0.01 s^{-1}. (a) Grain boundary map at strain of 0.4, (b) Local misorientation map of (a), (c) Changes in misorientation angle along the lines highlighted in (b), (d) Grain boundary map at strain of 0.5, (e) Local misorientation map of (d), (f) Changes in misorientation angle along the lines highlighted in (e), (g) Grain boundary map at strain of 0.9, (h) Local misorientation map of (g), (i) Changes in misorientation angle along the lines highlighted in (h). There, A1, B1, C1 lines represent along the grain, A2, B2, C2 lines represent within the grain. The green, blue, and black lines represent LAGBs, MAGBs, HAGBs, respectively.

3.5.3 Deformation temperature dynamic increase

Three characteristic sites a, b, and c in Fig. 5(a) were selected to study the microstructure development regulation mechanism during the deformation temperature dynamic increase. Fig. 18(a), (d), (g), and (b), (e), (h) show the GB maps and LocMis maps, respectively. Fig. 18(c), (f) and (i) show the corresponding misorientation angles along or within the grain. Fig. 18 depicts that the microstructure changed significantly with the deformation temperature dynamic increase. Fig. 18(a), (b) and (c) depict the position (strain of 0.4) before the deformation temperature dynamic increase. The original GB transitioned from the initial smooth GB state to the serrated state. There was a large number of LAGBs and MAGBs in the grain. Some newly generated DRX grains were nucleated by the grain boundary bulging mechanism of DDRX. The local and cumulative misorientation angle was less than 15°. The deformation temperature dynamic increased to 1100℃, as depicted in Fig. 18(d), (e) and (f). The number of LAGBs and MAGBs decreased and the DRX behavior was enhanced. The local and cumulative misorientation angle was less than 10°. This is because as the deformation continued, it increased the stored distortion energy and promoted the occurrence of DRX. In addition, with the deformation temperature dynamic increase, it enhanced the dislocation motion and promoted the migration of HAGBs. The DRX grains were still formed by the DDRX mechanism, and the newly generated DRX grains had less substructure with deformation proceeds at the deformation temperature of 1100℃ to a strain of 0.9, as depicted in Fig. 18(g), (h) and (i). The grain size became larger, and the local and cumulative misorientation angle was less than 5°. This suggests continuous deformation after the deformation temperature dynamic increase, which promotes the DRX and grain growth behavior with the coupled effect of stored distortion energy and thermal activation energy. Meanwhile, the increased deformation temperature increased the dislocation motion and lattice rotation and reduced cumulative misorientation [65]. Moreover, some LAGBs and MAGBs within the grains were still visible, indicating that a new cycle of DRX behavior was induced as the deformation proceed.

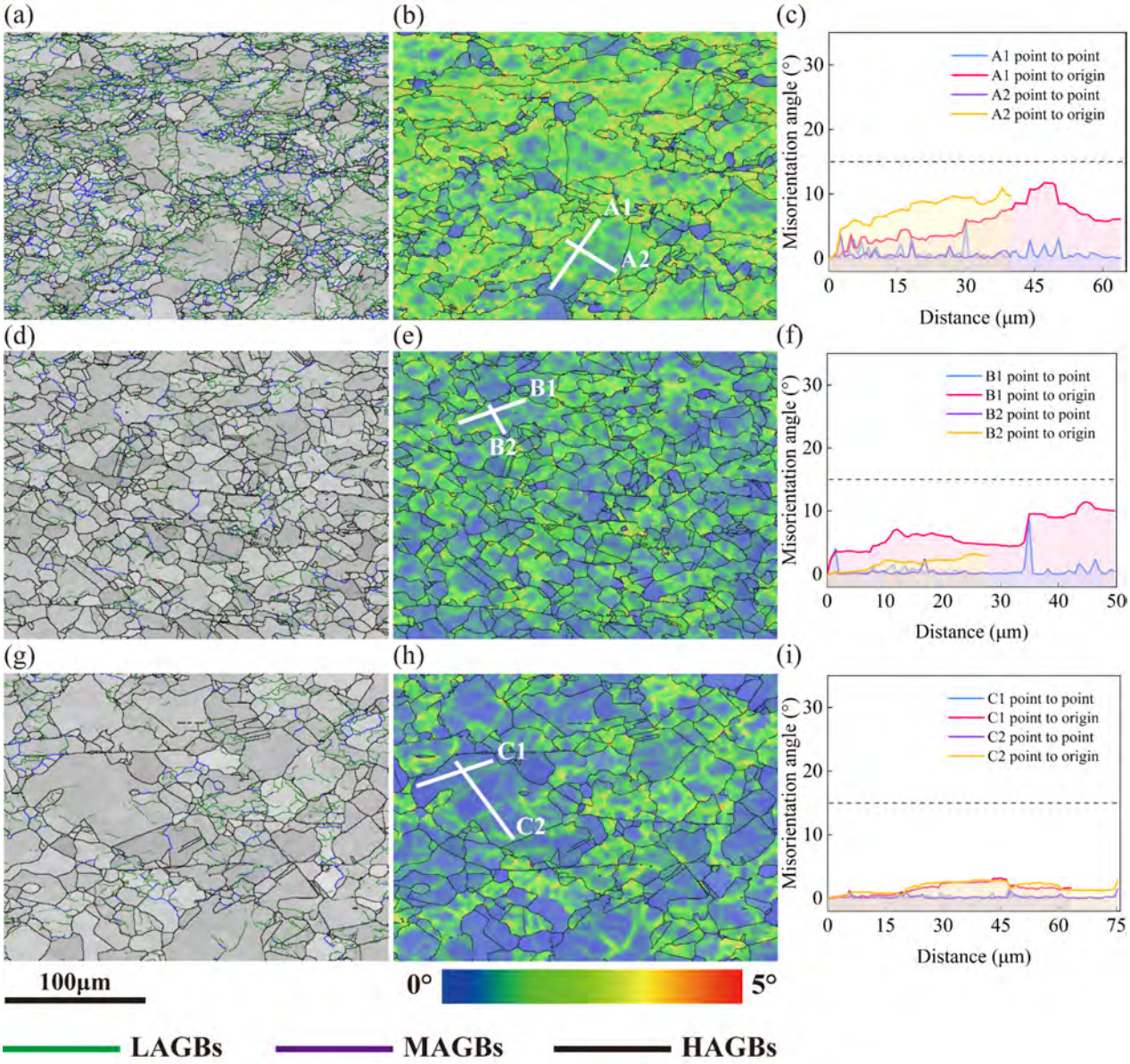

Fig. 18. Microstructure evolution at constant strain rate and deformation temperature dynamic increase from 1000°C to 1100°C. (a) Grain boundary map at strain of 0.4, (b) Local misorientation map of (a), (c) Changes in misorientation angle along the lines highlighted in (b), (d) Grain boundary map at strain of 0.5, (e) Local misorientation map of (d), (f) Changes in misorientation angle along the lines highlighted in (e), (g) Grain boundary map at strain of 0.9, (h) Local misorientation map of (g), (i) Changes in misorientation angle along the lines highlighted in (h). There, A1, B1, C1 lines represent along the grain, A2, B2, C2 lines represent within the grain. The green, blue, and black lines represent LAGBs, MAGBs, HAGBs, respectively.

3.5.4 Deformation temperature dynamic decrease

Three characteristic sites, a, b, and c in Fig. 5(b) were selected to study the microstructure development regulation mechanism during the deformation temperature dynamic decrease. Fig. 19(a), (d) and (g) show the GB maps. Fig. 19(b), (e) and (h) show the LocMis maps. Fig. 19(c), (f) and (i) show the misorientation angles along or within the grain. Fig. 19 illustrates that the microstructure changed less with the deformation temperature dynamic decrease. The position (strain of 0.4) before the deformation temperature dynamic decrease is shown in Fig. 19(a), (b) and (c). Owing to the samples deformed at a relatively high deformation temperature before the dynamic decrease state, the HAGBs migrated more easily and did not appear as relatively smooth GB as in the initial microstructure, but were distributed in a bulging mechanism of nucleation state, with fewer LAGBs and MAGBs inside the grain compared to the first

stage of deformation temperature dynamic increase state. As a result, the high temperature accelerated the dislocation rearrangement process, showing a low local and cumulative misorientation angle of less than 15°. As the deformation temperature dynamic decreased to 1000℃ (strain of 0.5), as depicted in Fig. 19(d), (e) and (f), the number of LAGBs and MAGBs increased. The reduced dislocation motion ability with the temperature dynamic decrease inhibited the migration of HAGBs. Although DRX nucleation was promoted as deformation continued, the deformation temperature dynamic decrease had an inhibiting effect on DRX grain growth, resulting in internal microscopic substructure evolution and without further grain growth. The local and cumulative misorientation angle was less than 15°, and the DRX was still nucleated by the mechanism of GB bulging. After the deformation temperature dynamic decreased deformed the sample to a strain of 0.9, as depicted in Fig. 19(g), (h) and (i). The volume fraction of DRX grains with smaller sizes increased, but the lower deformation temperature in the second stage suppressed the migration of GBs, resulting in smaller DRX grain sizes and a cumulative misorientation angle higher than 15°. It is worth noting that during the temperature dynamic decrease, the grain size did not increase compared to the deformation temperature dynamic increase state, but evolved in relatively uniform grain size. The number of LAGBs and MAGBs increased further, indicating that the lower deformation temperature promoted the emergence of the complicated and partially arranged substructures derived from dislocation walls.

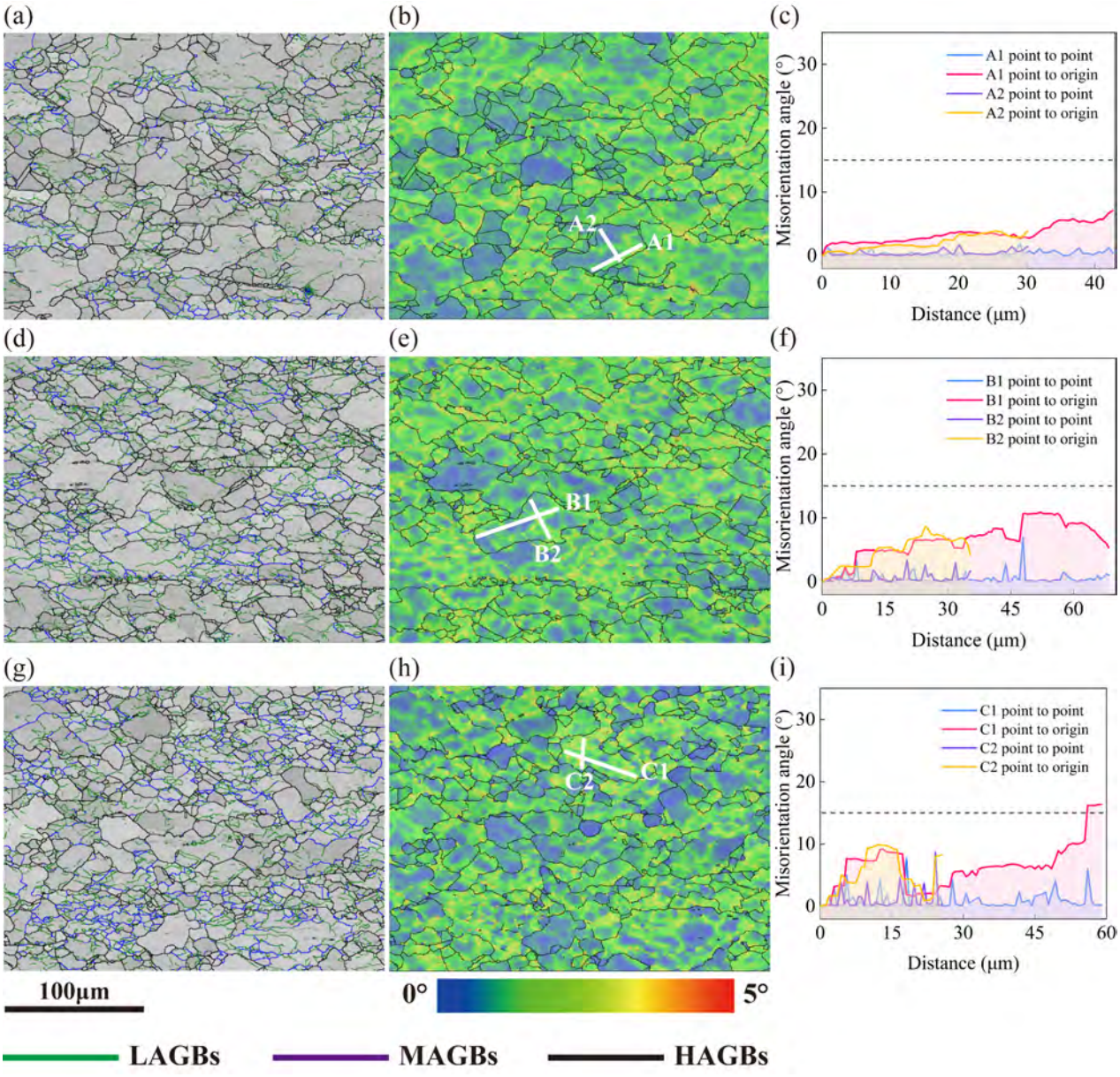

Fig. 19. Microstructure evolution at constant strain rate and deformation temperature dynamic decreased from 1100℃ to 1000℃. (a) Grain boundary map at strain of 0.4, (b) Local misorientation map of (a), (c) Changes in misorientation angle along the lines highlighted in (b), (d) Grain boundary map at strain of 0.5, (e) Local misorientation map of (d), (f) Changes in misorientation angle along the lines highlighted in (e), (g) Grain boundary map at strain of 0.9, (h) Local misorientation map of (g), (i) Changes in misorientation angle along the lines highlighted in (h). There, A1, B1, C1 lines represent along the grain, A2, B2, C2 lines represent within the grain. The green, blue, and black lines represent LAGBs, MAGBs, HAGBs, respectively.

3.6 Crystallographic orientation

Fig. 20 shows the inverse pole figure (IPF) and crystallographic orientation parallel to the ND of the strain rate transient variation deformed to different strains. It is evident from the figure that the microstructure, crystallographic orientation and pole density varied at different strains. The critical strains of DRX occurring at 1000℃ with the two strain rates were 0.12 and 0.18 as indicated in Fig. 7. This illustrates that the samples underwent DRX behavior prior to the strain rate transient variation, and the DRX volume fraction increased as the deformation proceeded. Furthermore, Fig. 20(a) shows that there was no obvious crystallographic orientation of the fiber along ND at a strain of 0.4. As the deformation process is a relatively unstable state, which is accompanied by GB migration, the distortion energy increased after the deformation. HAGBs had sufficient time to migrate at low initial strain rates, and DRX grains nucleated by the DDRX mechanism exhibited distinct rotational orientations, causing the GB to bulge and become more prominent in the high distortion region, mainly nucleated at serrated HAGBs by GB bulging and growing by GB migration. Therefore, with the DDRX mechanism, it is easier to obtain randomized crystallographic orientation, which is also consistent with the relevant literature [66]. When the strain rate dynamic increased to a strain of 0.5, the ⟨101⟩ fiber appeared. Since a certain number of primary deformed grains still existed in the microstructure at a strain of 0.5, resulting in a compression direction close to ⟨101⟩ fiber, the appearance of the ⟨101⟩ fiber at a strain of 0.5 is attributed to the existence of numerous strain-hardened grains in the matrix [67]. The ⟨111⟩ fiber appeared when the specimen deformed to the end. Although the aforementioned research indicates that the dislocation-free DRX grains have a randomized crystallographic orientation distribution, when the microstructure was incorporated into DRX grains, the fiber orientation rotated from ⟨101⟩ to ⟨111⟩ with deformation to a strain of 0.9. This means that the ⟨111⟩ fiber is a crystallographic orientation caused by the DRX grains. Interestingly, with the strain rate dynamic increase, the DRX grains were nucleated by the CDRX mechanism, and the dislocations of the CDRX process were rearranged to form new recrystallized grains, which inherit the parent orientation [68, 69]. The pole density was further increased compared to the strain of 0.4. Thus, it can be seen that the DDRX mechanism facilitated the randomness of crystallographic orientation. In addition, the trend of the pole density variation in Fig. 20(a) first increases then decreases. This is due to the deformation at the state of $0.01s^{-1}$, where the higher volume fraction of deformed grains that existed in the matrix was affected by strain hardening during hot deformation [70], resulting in an increasing pole density with strain increase. Meanwhile, the pole density near the ⟨101⟩ fiber is treated as a compression microtexture increased with strain, as described in other materials [71]. Hence, the crystallographic orientation parallel to ND favored the formation of the ⟨101⟩ fiber, which was caused by deformed grains in the matrix, while the crystallographic orientation driven by DRX grains tended to develop ⟨111⟩ fiber. In contrast, by comparing the two states of strain rate dynamic increase at a strain of 0.4 and 0.5. It was found that the pole density of 0.1 s^{-1} was higher than 0.01 s^{-1} state at a strain of 0.5, which is similar to fcc materials [72, 73]. Since the lower strain rate facilitated the occurrence of DRX, this exhibited a better random crystallographic orientation and weakened the pole density. Fig. 20(b) shows that the content of DRX after the strain rate dynamic decrease was larger before the transient variation initial state. A high strain rate before the transient variation accumulated a larger dislocation density for new grain nucleation, then the process of strain rate dynamic decrease provided sufficient duration for the development of new grains. Moreover, in both strain rate transient variation parts, numerous strain-hardened deformed grains in the matrix showed a crystallographic orientation close to the ⟨101⟩ fiber in the microstructure at a strain of 0.5. With deformation further

increased, the number of DRX grains increased and the ⟨101⟩ fiber pole density decreased. The strain of 0.4 showed a large pole density decrease before the strain rate dynamic decreased, as depicted in Fig. 20(b). From the prior section, it is clear that under the deformation condition, DRX was nucleated by the CDRX mechanism, which is not beneficial to form the random crystallographic orientation of the grains. The recrystallization mechanism shifted from CDRX to DDRX with the decrease in strain rate, which is more favorable to obtaining randomly crystallographic orientation grains.

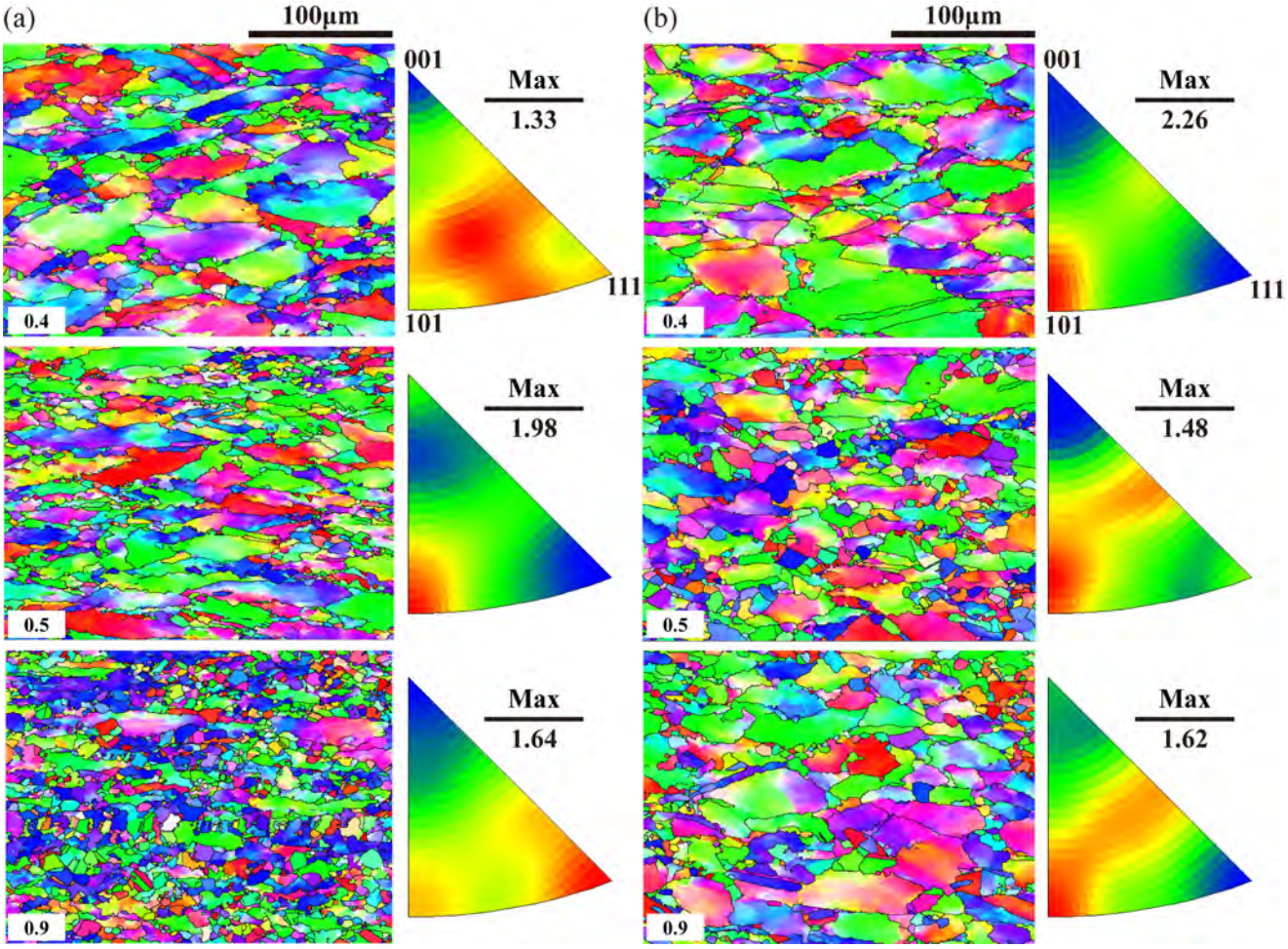

Fig. 20. Crystallographic orientation expressed by IPF at constant deformation temperature and transient strain rates of (a) 0.01 s^{-1} to 0.1 s^{-1}, (b) 0.1 s^{-1} to 0.01 s^{-1}

Fig. 21 depicts the IPF and crystallographic orientation parallel to the ND of the deformation temperature transient variation deformed to different strains. Since the deformation conditions of the samples at 0.01s^{-1} and deformation temperatures varied from 1000°C to 1100°C, the samples underwent different degrees of DRX before the temperature transient variation. It is evident from Fig. 21(a) that there was no significant crystallographic orientation of the sample before the deformation temperature dynamic increased (a strain of 0.4). With the temperature dynamic increased to 1100°C and deformed to a strain of 0.5 and 0.9, the thermal activation energy increased. Moreover, the stored distortion energy increased, and the DRX behavior intensified as the deformation continued. The sample underwent a significant DRX and grain growth. As discussed in the previous section, the ⟨111⟩ fiber was the DRX dominant crystallographic orientation. Therefore, the maximum pole density was in the ⟨111⟩ direction with deformation to a strain of 0.9. As illustrated in Fig. 21(b), the sample deformed to a strain of 0.4 before the deformation temperature dynamic decreased. The HAGBs migration behavior was stronger due to the initial deformation temperature of 1100°C in the first stage, which was higher than 1000°C in the first stage of Fig. 21(a), thus exhibiting a lower pole density. As the deformation temperature dynamic decreased to 1000°C, the sample deformed to a strain of 0.5. The DRX volume fraction in the

deformation temperature decreased state was higher than that in the increased state. Consequently, the ⟨111⟩ fiber representing the dominant DRX crystallographic orientation intensified when the sample deformed to a strain of 0.5. The pole density was also higher than the value of the dynamic increase in deformation temperature. It is noteworthy that the deformation temperature dynamic decreased to a strain of 0.9, showing that the crystallographic orientation of the strain-hardened grains ⟨101⟩ fiber was sharpened. This is attributed to the possible induction of a new round of recrystallization behavior as the deformation proceeded during the deformation temperature dynamic decrease. Therefore, the presence of deformed (strain-hardened) grains in the matrix is beneficial to form crystallographic orientation in the ⟨101⟩ fiber.

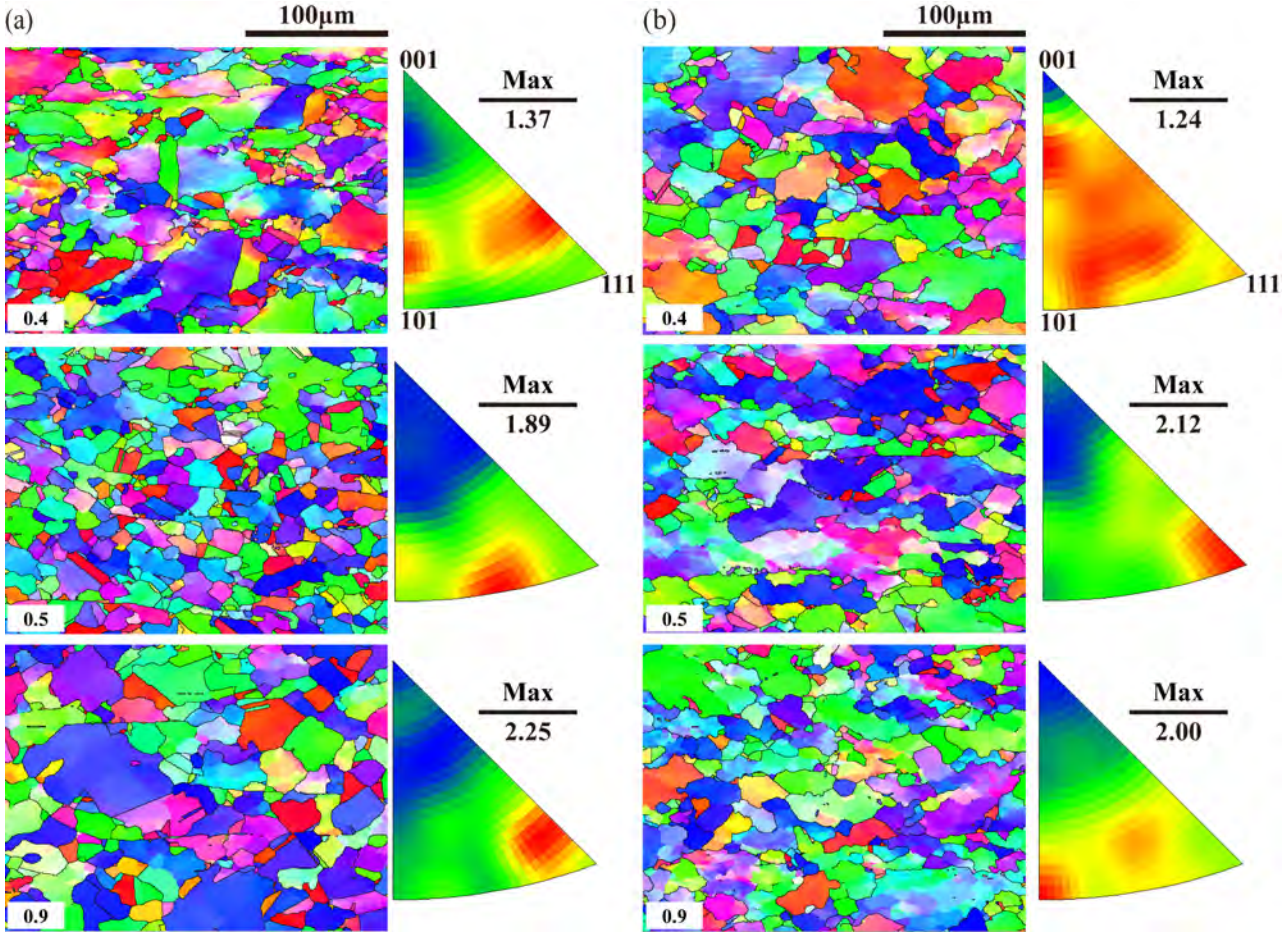

Fig. 21. Crystallographic orientations at the deformation temperature of (a) 1000℃ to 1100℃, (b) 1100℃ to 1000℃.

4. Conclusions

The flow stress and hot workability of the experimental steel at constant and transient deformation states were studied based on systematic experimental data. The strain rate transient deformation state takes a different strain interval for the flow stress curves to evolve to a state that deforms to the same accumulated deformation level at a constant strain rate and the flow stress rapidly adjusts and then gradually reaches a new stress level under a transient deformation state. DRX is the primary softening behavior among all deformation states, and the critical stress under a constant deformation state can be determined using the WH rate and flow stress curves. Considering the effect of DRV, a DRX kinetic model was developed that can predict DRX volume fraction and flow stress more accurately under constant and transient deformation states. The 3D HPM was established with different deformation parameters for the studied steel. The microstructure evolution mechanism confirms the accuracy of the established HPM stable and instability areas.

In addition, the microstructure and crystallographic orientation caused by the transient deformation state were

investigated. The microstructure development is controlled by two principal DRX mechanisms during the strain rate transient variation state: the strain rate dynamic increase will cause the DRX mechanism to shift from DDRX to CDRX; conversely, the DRX mechanism will shift from CDRX to DDRX when the strain rate dynamic decreases. The deformation temperature dynamic decrease is beneficial to obtaining uniform grain size. The ⟨101⟩ fiber and ⟨111⟩ fiber are compressed and have a recrystallized crystal orientation parallel to ND. The DDRX recrystallization mechanism lead to the random orientation of the grains under strain rate dynamic change state.

Acknowledgments

This work was supported by Regional Joint Funds of the National Natural Science Foundation of China (Grant No. U20A20289); Innovative Research Groups Project of the Natural Science Foundation of Hebei Province (Grant No. E2021203011); Central Guidance on Local Science and Technology Development Funding Project (Grant No. 206Z1601G).

References

[1] X. Han, L. Hua, L. Peng, W. Feng, An innovative radial envelope forming method for manufacturing thin-walled cylindrical ring with inner web ribs, Journal of Materials Processing Technology, 286 (2020) 116836.

[2] C. Liu, S. Barella, Y. Peng, J. Sun, S. Guo, S. Liang, A. Gruttadauria, C. Mapelli, Dynamic recrystallization behavior under steady and transient mutation deformation state, Materials Science and Engineering: A, 843 (2022) 143138.

[3] X. Han, L. Hua, S. Yang, A novel polygonal ring rolling method, Journal of Manufacturing Processes, 59 (2020) 389-402.

[4] K. Huang, R.E. Logé, Microstructure and flow stress evolution during hot deformation of 304L austenitic stainless steel in variable thermomechanical conditions, Materials Science and Engineering: A, 711 (2018) 600-610.

[5] C. Li, L. Huang, M. Zhao, X. Zhang, J. Li, P. Li, Influence of hot deformation on dynamic recrystallization behavior of 300M steel: Rules and modeling, Materials Science and Engineering: A, 797 (2020) 139925.

[6] M. Zhao, L. Huang, C. Li, J. Li, P. Li, Evaluation of the deformation behaviors and hot workability of a high-strength low-alloy steel, Materials Science and Engineering A, 810 (2021).

[7] J. Zhang, Y. Yi, S. Huang, X. Mao, H. He, J. Tang, W. Guo, F. Dong, Dynamic recrystallization mechanisms of 2195 aluminum alloy during medium/high temperature compression deformation, Materials Science and Engineering: A, 804 (2021) 140650.

[8] Y.-W. Xiao, Y.C. Lin, Y.-Q. Jiang, X.-Y. Zhang, G.-D. Pang, D. Wang, K.-C. Zhou, A dislocation density-based model and processing maps of Ti-55511 alloy with bimodal microstructures during hot compression in α+β region, Materials Science and Engineering: A, 790 (2020) 139692.

[9] C.M. Sellars, Modelling microstructural development during hot rolling, Materials Science and Technology, 6 (1990) 1072-1081.

[10] C.M. Sellars, J.A. Whiteman, Recrystallization and grain growth in hot rolling, Metal Science, 13 (1979) 187-194.

[11] T. Senuma, H. Yada, H. Yoshimura, H. Harada, S. Hamauzu, Deformation Resistance and Recrystallization of Commercially Pure Titanium in the High Strain Rate Hot Deformation, Tetsu-to-Hagane, 72 (1986) 321-328.

[12] S.-I. Kim, Y. Lee, D.-L. Lee, Y.-C. Yoo, Modeling of AGS and recrystallized fraction of microalloyed medium carbon steel during hot deformation, Materials Science and Engineering: A, 355 (2003) 384-393.

[13] S.-I. Kim, Y.-C. Yoo, Dynamic recrystallization behavior of AISI 304 stainless steel, Materials Science and Engineering: A, 311 (2001) 108-113.

[14] J. Liu, Z. Cui, L. Ruan, A new kinetics model of dynamic recrystallization for magnesium alloy AZ31B, Materials Science and Engineering: A, 529 (2011) 300-310.

[15] T. Sakai, A. Belyakov, R. Kaibyshev, H. Miura, J.J. Jonas, Dynamic and post-dynamic recrystallization under hot, cold and severe plastic deformation conditions, Progress in materials science, 60 (2014) 130-207.

[16] C. Ghosh, C. Aranas Jr, J.J. Jonas, Dynamic transformation of deformed austenite at temperatures above the Ae3, Progress in Materials Science, 82 (2016) 151-233.

[17] M. Frommert, G. Gottstein, Mechanical behavior and microstructure evolution during steady-state dynamic recrystallization in the austenitic steel 800H, Materials Science and Engineering: A, 506 (2009) 101-110.
[18] K. Graetz, C. Miessen, G. Gottstein, Analysis of steady-state dynamic recrystallization, Acta Materialia, 67 (2014) 58-66.
[19] W. Chen, B. Hu, C. Jia, C. Zheng, D. Li, Continuous dynamic recrystallization during the transient deformation in a Ni-30%Fe austenitic model alloy, Materials Science and Engineering A, 751 (2019) 10-14.
[20] M. Wang, C. Sun, M.W. Fu, Z. Liu, C. Wang, Experimental investigations and constitutive modeling of the dynamic recrystallization behavior of Inconel 740 superalloy, Materials Science and Engineering: A, 793 (2020) 139939.
[21] S. Kumar, D. Samantaray, B. Aashranth, N. Keskar, M.A. Davinci, U. Borah, D. Srivastava, A.K. Bhaduri, Dependency of rate sensitive DRX behaviour on interstitial content of a Fe-Cr-Ni-Mo alloy, Materials Science and Engineering: A, 743 (2019) 148-158.
[22] K.S. Cho, H.S. Sim, J.H. Kim, J.H. Choi, K.B. Lee, H.R. Yang, H. Kwon, A novel etchant for revealing the prior austenite grain boundaries and matrix information in high alloy steels, Materials Characterization, 59 (2008) 786-793.
[23] Z.R. Zeng, Y.M. Zhu, S.W. Xu, M.Z. Bian, C.H.J. Davies, N. Birbilis, J.F. Nie, Texture evolution during static recrystallization of cold-rolled magnesium alloys, Acta Materialia, 105 (2016) 479-494.
[24] J.J. Urcola, C.M. Sellars, Influence of changing strain rate on microstructure during hot deformation, Acta Metallurgica, 35 (1987) 2649-2657.
[25] X.-M. Chen, Y.C. Lin, X.-H. Li, M.-S. Chen, W.-Q. Yuan, Investigation on strain dependence of metadynamic recrystallization behaviors of GH4169 superalloy, Vacuum, 149 (2018) 1-11.
[26] R. Motallebi, Z. Savaedi, H. Mirzadeh, Additive manufacturing – A review of hot deformation behavior and constitutive modeling of flow stress, Current Opinion in Solid State and Materials Science, 26 (2022) 100992.
[27] E.S. Puchi-Cabrera, M.H. Staia, J.D. Guérin, J. Lesage, M. Dubar, D. Chicot, An experimental analysis and modeling of the work-softening transient due to dynamic recrystallization, International Journal of Plasticity, 54 (2014) 113-131.
[28] J.P.A. Immarigeon, J.J. Jonas, Flow stress and substructural change during the transient deformation of Armco iron and silicon steel, Acta Metallurgica, 19 (1971) 1053-1061.
[29] H. Mirzadeh, A. Najafizadeh, Prediction of the critical conditions for initiation of dynamic recrystallization, Materials & Design, 31 (2010) 1174-1179.
[30] C. Liu, C. Mapelli, Y. Peng, S. Barella, S. Liang, A. Gruttadauria, M. Belfi, Dynamic Recrystallization Behavior of Low-Carbon Steel during the Flexible Rolling Process: Modeling and Characterization, steel research international, 93 (2022) 2100490.
[31] C. Liu, Y. Peng, S. Barella, C. Mapelli, S. Liang, Characterization of dynamic recrystallization behavior of low carbon steel under flexible rolling process, Materials Today Communications, 29 (2021) 102777.
[32] E.I. Poliak, J.J. Jonas, A one-parameter approach to determining the critical conditions for the initiation of dynamic recrystallization, Acta Materialia, 44 (1996) 127-136.
[33] Y. Han, H. Wu, W. Zhang, D. Zou, G. Liu, G. Qiao, Constitutive equation and dynamic recrystallization behavior of as-cast 254SMO super-austenitic stainless steel, Materials and Design, 69 (2015) 230-240.
[34] J.S. Nagra, A. Brahme, J. Lévesque, R. Mishra, R.A. Lebensohn, K. Inal, A new micromechanics based full field numerical framework to simulate the effects of dynamic recrystallization on the formability of HCP metals, International Journal of Plasticity, 125 (2020) 210-234.
[35] Q. Luo, Y. Guo, B. Liu, Y. Feng, J. Zhang, Q. Li, K. Chou, Thermodynamics and kinetics of phase transformation in rare earth–magnesium alloys: A critical review, Journal of Materials Science and Technology, 44 (2020) 171-190.
[36] P. Gao, M. Fu, M. Zhan, Z. Lei, Y. Li, Deformation behavior and microstructure evolution of titanium alloys with lamellar microstructure in hot working process: A review, Journal of Materials Science and Technology, 39 (2020) 56-73.
[37] Y. Wang, J. Wang, J. Dong, A. Li, Z. Li, G. Xie, L. Lou, Hot deformation characteristics and hot working window of as-cast large-tonnage GH3535 superalloy ingot, Journal of Materials Science and Technology, 34 (2018) 2439-2446.

[38] Y. Wang, J. Li, Y. Xin, C. Li, Y. Cheng, X. Chen, M. Rashad, B. Liu, Y. Liu, Effect of Zener–Hollomon parameter on hot deformation behavior of CoCrFeMnNiC0.5 high entropy alloy, Materials Science and Engineering: A, 768 (2019) 138483.
[39] Z. Savaedi, R. Motallebi, H. Mirzadeh, A review of hot deformation behavior and constitutive models to predict flow stress of high-entropy alloys, Journal of Alloys and Compounds, 903 (2022) 163964.
[40] N.D. Ryan, H.J. McQueen, Flow stress, dynamic restoration, strain hardening and ductility in hot working of 316 steel, Journal of Materials Processing Technology, 21 (1990) 177-199.
[41] S.H. Zahiri, C.H.J. Davies, P.D. Hodgson, A mechanical approach to quantify dynamic recrystallization in polycrystalline metals, Scripta Materialia, 52 (2005) 299-304.
[42] J. Liu, Z. Cui, L. Ruan, A new kinetics model of dynamic recrystallization for magnesium alloy AZ31B, Materials Science and Engineering A, 529 (2011) 300-310.
[43] S. Gardner, W. Li, M. Coleman, R. Johnston, The effects of thermomechanical history on the microstructure of a nickel-base superalloy during forging, Materials Science and Engineering A, 668 (2016) 263-270.
[44] J.J. Jonas, X. Quelennec, L. Jiang, É. Martin, The Avrami kinetics of dynamic recrystallization, Acta materialia, 57 (2009) 2748-2756.
[45] A.I. Fernández, P. Uranga, B. López, J.M. Rodriguez-Ibabe, Dynamic recrystallization behavior covering a wide austenite grain size range in Nb and Nb-Ti microalloyed steels, Materials Science and Engineering A, 361 (2003) 367-376.
[46] M.H. Wang, Y.F. Li, W.H. Wang, J. Zhou, A. Chiba, Quantitative Analysis of Work Hardening and Dynamic Softening Behavior of low carbon alloy Steel Based on the Flow Stress, Materials and Design, 45 (2013) 384-392.
[47] A. Marandi, A. Zarei-Hanzaki, N. Haghdadi, M. Eskandari, The prediction of hot deformation behavior in Fe-21Mn-2.5Si-1.5Al transformation-twinning induced plasticity steel, Materials Science and Engineering A, 554 (2012) 72-78.
[48] E.S. Puchi-Cabrera, J.D. Guérin, M. Dubar, L. Dubar, A. Dubois, A novel approach for modeling the flow stress curves of austenite under transient deformation conditions, Materials Science and Engineering: A, 673 (2016) 660-670.
[49] E.S. Puchi-Cabrera, J.-D. Guérin, M. Dubar, M.H. Staia, J. Lesage, D. Chicot, Constitutive description for the design of hot-working operations of a 20MnCr5 steel grade, Materials & Design (1980-2015), 62 (2014) 255-264.
[50] E.S. Puchi-Cabrera, J.D. Guérin, M. Dubar, M.H. Staia, J. Lesage, D. Chicot, Constitutive description of Fe–Mn23–C0.6 steel deformed under hot-working conditions, International Journal of Mechanical Sciences, 99 (2015) 143-153.
[51] I. Schindler, P. Kawulok, R. Kawulok, E. Hadasik, D. Kuc, Influence of Calculation Method on Value of Activation Energy in Hot Forming, High Temperature Materials and Processes, 32 (2013) 149-155.
[52] Y. Sun, Z. Wan, L. Hu, J. Ren, Characterization of hot processing parameters of powder metallurgy TiAl-based alloy based on the activation energy map and processing map, Materials & Design, 86 (2015) 922-932.
[53] D.-X. Wen, Y.C. Lin, H.-B. Li, X.-M. Chen, J. Deng, L.-T. Li, Hot deformation behavior and processing map of a typical Ni-based superalloy, Materials Science and Engineering: A, 591 (2014) 183-192.
[54] E. Pu, W. Zheng, J. Xiang, Z. Song, J. Li, Hot deformation characteristic and processing map of superaustenitic stainless steel S32654, Materials Science and Engineering: A, 598 (2014) 174-182.
[55] S.V.S. Narayana Murty, B. Nageswara Rao, B.P. Kashyap, Instability criteria for hot deformation of materials, International Materials Reviews, 45 (2000) 15-26.
[56] X. Zhang, Q. Yan, C. Yang, T. Wang, C. Ge, Microstructure, mechanical properties and bonding characteristic of deformed tungsten, International Journal of Refractory Metals and Hard Materials, 43 (2014) 302-308.
[57] Y. Prasad, H. Gegel, S. Doraivelu, J. Malas, J. Morgan, K. Lark, D. Barker, Modeling of dynamic material behavior in hot deformation: forging of Ti-6242, Metallurgical Transactions A, 15 (1984) 1883-1892.
[58] E. Pu, W. Zheng, Z. Song, H. Feng, H. Dong, Hot deformation characterization of nickel-based superalloy UNS10276 through processing map and microstructural studies, Journal of Alloys and Compounds, 694 (2017) 617-631.
[59] F. Zhang, J.L. Sun, J. Shen, X.D. Yan, J. Chen, Flow behavior and processing maps of 2099 alloy, Materials Science and Engineering A, 613 (2014) 141-147.

[60] Y.V.R.K. Prasad, T. Seshacharyulu, Processing maps for hot working of titanium alloys, Materials Science and Engineering A, 243 (1998) 82-88.
[61] A. Jenab, A. Karimi Taheri, Experimental investigation of the hot deformation behavior of AA7075: Development and comparison of flow localization parameter and dynamic material model processing maps, International Journal of Mechanical Sciences, 78 (2014) 97-105.
[62] S. Gourdet, F. Montheillet, A model of continuous dynamic recrystallization, Acta Materialia, 51 (2003) 2685-2699.
[63] J. Lv, J.-H. Zheng, V.A. Yardley, Z. Shi, J. Lin, A Review of Microstructural Evolution and Modelling of Aluminium Alloys under Hot Forming Conditions, Metals, 10 (2020).
[64] Y. Ito, Z. Horita, Microstructural evolution in pure aluminum processed by high-pressure torsion, Materials Science and Engineering: A, 503 (2009) 32-36.
[65] Y.C. Lin, X.-Y. Wu, X.-M. Chen, J. Chen, D.-X. Wen, J.-L. Zhang, L.-T. Li, EBSD study of a hot deformed nickel-based superalloy, Journal of Alloys and Compounds, 640 (2015) 101-113.
[66] M.G. Jiang, C. Xu, H. Yan, G.H. Fan, T. Nakata, C.S. Lao, R.S. Chen, S. Kamado, E.H. Han, B.H. Lu, Unveiling the formation of basal texture variations based on twinning and dynamic recrystallization in AZ31 magnesium alloy during extrusion, Acta Materialia, 157 (2018) 53-71.
[67] A.M. Wusatowska-Sarnek, H. Miura, T. Sakai, Nucleation and microtexture development under dynamic recrystallization of copper, Materials Science and Engineering: A, 323 (2002) 177-186.
[68] D.H. Qin, M.J. Wang, C.Y. Sun, Z.X. Su, L.Y. Qian, Z.H. Sun, Interaction between texture evolution and dynamic recrystallization of extruded AZ80 magnesium alloy during hot deformation, Materials Science and Engineering: A, 788 (2020) 139537.
[69] R. Peng, C. Xu, Y. Li, S. Zhong, X. Cao, Y. Ding, Multiple-twinning induced recrystallization and texture optimization in a differential-temperature-rolled AZ31B magnesium alloy with excellent ductility, Materials Research Letters, 10 (2022) 318-326.
[70] R.R. Eleti, T. Bhattacharjee, A. Shibata, N. Tsuji, Unique deformation behavior and microstructure evolution in high temperature processing of HfNbTaTiZr refractory high entropy alloy, Acta Materialia, 171 (2019) 132-145.
[71] M. Hasegawa, M. Yamamoto, H. Fukutomi, Formation mechanism of texture during dynamic recrystallization in γ-TiAl, nickel and copper examined by microstructure observation and grain boundary analysis based on local orientation measurements, Acta Materialia, 51 (2003) 3939-3950.
[72] S.P. Coryell, K.O. Findley, M.C. Mataya, E. Brown, Evolution of Microstructure and Texture During Hot Compression of a Ni-Fe-Cr Superalloy, Metallurgical and Materials Transactions A, 43 (2012) 633-649.
[73] M. Rezayat, M.H. Parsa, H. Mirzadeh, J.M. Cabrera, Texture development during hot deformation of Al/Mg alloy reinforced with ceramic particles, Journal of Alloys and Compounds, 798 (2019) 267-272.